BABAR-PUB-10/06
SLAC-PUB-14181

Search for $b \to u$ Transitions in $B^- \to DK^-$ and D^*K^- Decays

P. del Amo Sanchez,[1] J. P. Lees,[1] V. Poireau,[1] E. Prencipe,[1] V. Tisserand,[1] J. Garra Tico,[2] E. Grauges,[2] M. Martinelli[ab],[3] A. Palano[ab],[3] M. Pappagallo[ab],[3] G. Eigen,[4] B. Stugu,[4] L. Sun,[4] M. Battaglia,[5] D. N. Brown,[5] B. Hooberman,[5] L. T. Kerth,[5] Yu. G. Kolomensky,[5] G. Lynch,[5] I. L. Osipenkov,[5] T. Tanabe,[5] C. M. Hawkes,[6] A. T. Watson,[6] H. Koch,[7] T. Schroeder,[7] D. J. Asgeirsson,[8] C. Hearty,[8] T. S. Mattison,[8] J. A. McKenna,[8] A. Khan,[9] A. Randle-Conde,[9] V. E. Blinov,[10] A. R. Buzykaev,[10] V. P. Druzhinin,[10] V. B. Golubev,[10] A. P. Onuchin,[10] S. I. Serednyakov,[10] Yu. I. Skovpen,[10] E. P. Solodov,[10] K. Yu. Todyshev,[10] A. N. Yushkov,[10] M. Bondioli,[11] S. Curry,[11] D. Kirkby,[11] A. J. Lankford,[11] M. Mandelkern,[11] E. C. Martin,[11] D. P. Stoker,[11] H. Atmacan,[12] J. W. Gary,[12] F. Liu,[12] O. Long,[12] G. M. Vitug,[12] C. Campagnari,[13] T. M. Hong,[13] D. Kovalskyi,[13] J. D. Richman,[13] A. M. Eisner,[14] C. A. Heusch,[14] J. Kroseberg,[14] W. S. Lockman,[14] A. J. Martinez,[14] T. Schalk,[14] B. A. Schumm,[14] A. Seiden,[14] L. O. Winstrom,[14] C. H. Cheng,[15] D. A. Doll,[15] B. Echenard,[15] D. G. Hitlin,[15] P. Ongmongkolkul,[15] F. C. Porter,[15] A. Y. Rakitin,[15] R. Andreassen,[16] M. S. Dubrovin,[16] G. Mancinelli,[16] B. T. Meadows,[16] M. D. Sokoloff,[16] P. C. Bloom,[17] W. T. Ford,[17] A. Gaz,[17] J. F. Hirschauer,[17] M. Nagel,[17] U. Nauenberg,[17] J. G. Smith,[17] S. R. Wagner,[17] R. Ayad,[18,*] W. H. Toki,[18] H. Jasper,[19] T. M. Karbach,[19] J. Merkel,[19] A. Petzold,[19] B. Spaan,[19] K. Wacker,[19] M. J. Kobel,[20] K. R. Schubert,[20] R. Schwierz,[20] D. Bernard,[21] M. Verderi,[21] P. J. Clark,[22] S. Playfer,[22] J. E. Watson,[22] M. Andreotti[ab],[23] D. Bettoni[a],[23] C. Bozzi[a],[23] R. Calabrese[ab],[23] A. Cecchi[ab],[23] G. Cibinetto[ab],[23] E. Fioravanti[ab],[23] P. Franchini[ab],[23] E. Luppi[ab],[23] M. Munerato[ab],[23] M. Negrini[ab],[23] A. Petrella[ab],[23] L. Piemontese[a],[23] R. Baldini-Ferroli,[24] A. Calcaterra,[24] R. de Sangro,[24] G. Finocchiaro,[24] M. Nicolaci,[24] S. Pacetti,[24] P. Patteri,[24] I. M. Peruzzi,[24,†] M. Piccolo,[24] M. Rama,[24] A. Zallo,[24] R. Contri[ab],[25] E. Guido[ab],[25] M. Lo Vetere[ab],[25] M. R. Monge[ab],[25] S. Passaggio[a],[25] C. Patrignani[ab],[25] E. Robutti[a],[25] S. Tosi[ab],[25] B. Bhuyan,[26] C. L. Lee,[27] M. Morii,[27] A. Adametz,[28] J. Marks,[28] S. Schenk,[28] U. Uwer,[28] F. U. Bernlochner,[29] M. Ebert,[29] H. M. Lacker,[29] T. Lueck,[29] A. Volk,[29] P. D. Dauncey,[30] M. Tibbetts,[30] P. K. Behera,[31] U. Mallik,[31] C. Chen,[32] J. Cochran,[32] H. B. Crawley,[32] L. Dong,[32] W. T. Meyer,[32] S. Prell,[32] E. I. Rosenberg,[32] A. E. Rubin,[32] Y. Y. Gao,[33] A. V. Gritsan,[33] Z. J. Guo,[33] N. Arnaud,[34] M. Davier,[34] D. Derkach,[34] J. Firmino da Costa,[34] G. Grosdidier,[34] F. Le Diberder,[34] A. M. Lutz,[34] B. Malaescu,[34] A. Perez,[34] P. Roudeau,[34] M. H. Schune,[34] J. Serrano,[34] V. Sordini,[34,‡] A. Stocchi,[34] L. Wang,[34] G. Wormser,[34] D. J. Lange,[35] D. M. Wright,[35] I. Bingham,[36] J. P. Burke,[36] C. A. Chavez,[36] J. P. Coleman,[36] J. R. Fry,[36] E. Gabathuler,[36] R. Gamet,[36] D. E. Hutchcroft,[36] D. J. Payne,[36] C. Touramanis,[36] A. J. Bevan,[37] F. Di Lodovico,[37] R. Sacco,[37] M. Sigamani,[37] G. Cowan,[38] S. Paramesvaran,[38] A. C. Wren,[38] D. N. Brown,[39] C. L. Davis,[39] A. G. Denig,[40] M. Fritsch,[40] W. Gradl,[40] A. Hafner,[40] K. E. Alwyn,[41] D. Bailey,[41] R. J. Barlow,[41] G. Jackson,[41] G. D. Lafferty,[41] T. J. West,[41] J. Anderson,[42] R. Cenci,[42] A. Jawahery,[42] D. A. Roberts,[42] G. Simi,[42] J. M. Tuggle,[42] C. Dallapiccola,[43] E. Salvati,[43] R. Cowan,[44] D. Dujmic,[44] P. H. Fisher,[44] G. Sciolla,[44] M. Zhao,[44] D. Lindemann,[45] P. M. Patel,[45] S. H. Robertson,[45] M. Schram,[45] P. Biassoni[ab],[46] A. Lazzaro[ab],[46] V. Lombardo[a],[46] F. Palombo[ab],[46] S. Stracka[ab],[46] L. Cremaldi,[47] R. Godang,[47,§] R. Kroeger,[47] P. Sonnek,[47] D. J. Summers,[47] X. Nguyen,[48] M. Simard,[48] P. Taras,[48] G. De Nardo[ab],[49] D. Monorchio[ab],[49] G. Onorato[ab],[49] C. Sciacca[ab],[49] G. Raven,[50] H. L. Snoek,[50] C. P. Jessop,[51] K. J. Knoepfel,[51] J. M. LoSecco,[51] W. F. Wang,[51] L. A. Corwin,[52] K. Honscheid,[52] R. Kass,[52] J. P. Morris,[52] A. M. Rahimi,[52] N. L. Blount,[53] J. Brau,[53] R. Frey,[53] O. Igonkina,[53] J. A. Kolb,[53] R. Rahmat,[53] N. B. Sinev,[53] D. Strom,[53] J. Strube,[53] E. Torrence,[53] G. Castelli[ab],[54] E. Feltresi[ab],[54] N. Gagliardi[ab],[54] M. Margoni[ab],[54] M. Morandin[a],[54] M. Posocco[a],[54] M. Rotondo[a],[54] F. Simonetto[ab],[54] R. Stroili[ab],[54] E. Ben-Haim,[55] G. R. Bonneaud,[55] H. Briand,[55] G. Calderini,[55] J. Chauveau,[55] O. Hamon,[55] Ph. Leruste,[55] G. Marchiori,[55] J. Ocariz,[55] J. Prendki,[55] S. Sitt,[55] M. Biasini[ab],[56] E. Manoni[ab],[56] C. Angelini[ab],[57] G. Batignani[ab],[57] S. Bettarini[ab],[57] M. Carpinelli[ab],[57,¶] G. Casarosa[ab],[57] A. Cervelli[ab],[57] F. Forti[ab],[57] M. A. Giorgi[ab],[57] A. Lusiani[ac],[57] N. Neri[ab],[57] E. Paoloni[ab],[57] G. Rizzo[ab],[57] J. J. Walsh[a],[57] D. Lopes Pegna,[58] C. Lu,[58] J. Olsen,[58] A. J. S. Smith,[58] A. V. Telnov,[58] F. Anulli[a],[59] E. Baracchini[ab],[59] G. Cavoto[a],[59] R. Faccini[ab],[59] F. Ferrarotto[a],[59] F. Ferroni[ab],[59] M. Gaspero[ab],[59] L. Li Gioi[a],[59] M. A. Mazzoni[a],[59] G. Piredda[a],[59] F. Renga[ab],[59] T. Hartmann,[60] T. Leddig,[60] H. Schröder,[60] R. Waldi,[60] T. Adye,[61] B. Franek,[61] E. O. Olaiya,[61] F. F. Wilson,[61] S. Emery,[62] G. Hamel de Monchenault,[62] G. Vasseur,[62] Ch. Yèche,[62] M. Zito,[62] M. T. Allen,[63] D. Aston,[63] D. J. Bard,[63] R. Bartoldus,[63] J. F. Benitez,[63] C. Cartaro,[63] M. R. Convery,[63] J. Dorfan,[63] G. P. Dubois-Felsmann,[63] W. Dunwoodie,[63] R. C. Field,[63] M. Franco Sevilla,[63] B. G. Fulsom,[63]

Work supported in part by US Department of Energy contract DE-AC02-76SF00515.

A. M. Gabareen,[63] M. T. Graham,[63] P. Grenier,[63] C. Hast,[63] W. R. Innes,[63] M. H. Kelsey,[63] H. Kim,[63] P. Kim,[63] M. L. Kocian,[63] D. W. G. S. Leith,[63] S. Li,[63] B. Lindquist,[63] S. Luitz,[63] V. Luth,[63] H. L. Lynch,[63] D. B. MacFarlane,[63] H. Marsiske,[63] D. R. Muller,[63] H. Neal,[63] S. Nelson,[63] C. P. O'Grady,[63] I. Ofte,[63] M. Perl,[63] T. Pulliam,[63] B. N. Ratcliff,[63] A. Roodman,[63] A. A. Salnikov,[63] V. Santoro,[63] R. H. Schindler,[63] J. Schwiening,[63] A. Snyder,[63] D. Su,[63] M. K. Sullivan,[63] S. Sun,[63] K. Suzuki,[63] J. M. Thompson,[63] J. Va'vra,[63] A. P. Wagner,[63] M. Weaver,[63] C. A. West,[63] W. J. Wisniewski,[63] M. Wittgen,[63] D. H. Wright,[63] H. W. Wulsin,[63] A. K. Yarritu,[63] C. C. Young,[63] V. Ziegler,[63] X. R. Chen,[64] W. Park,[64] M. V. Purohit,[64] R. M. White,[64] J. R. Wilson,[64] S. J. Sekula,[65] M. Bellis,[66] P. R. Burchat,[66] A. J. Edwards,[66] T. S. Miyashita,[66] S. Ahmed,[67] M. S. Alam,[67] J. A. Ernst,[67] B. Pan,[67] M. A. Saeed,[67] S. B. Zain,[67] N. Guttman,[68] A. Soffer,[68] P. Lund,[69] S. M. Spanier,[69] R. Eckmann,[70] J. L. Ritchie,[70] A. M. Ruland,[70] C. J. Schilling,[70] R. F. Schwitters,[70] B. C. Wray,[70] J. M. Izen,[71] X. C. Lou,[71] F. Bianchi[ab],[72] D. Gamba[ab],[72] M. Pelliccioni[ab],[72] M. Bomben[ab],[73] L. Lanceri[ab],[73] L. Vitale[ab],[73] N. Lopez-March,[74] F. Martinez-Vidal,[74] D. A. Milanes,[74] A. Oyanguren,[74] J. Albert,[75] Sw. Banerjee,[75] H. H. F. Choi,[75] K. Hamano,[75] G. J. King,[75] R. Kowalewski,[75] M. J. Lewczuk,[75] I. M. Nugent,[75] J. M. Roney,[75] R. J. Sobie,[75] T. J. Gershon,[76] P. F. Harrison,[76] J. Ilic,[76] T. E. Latham,[76] E. M. T. Puccio,[76] H. R. Band,[77] S. Dasu,[77] K. T. Flood,[77] Y. Pan,[77] R. Prepost,[77] C. O. Vuosalo,[77] and S. L. Wu[77]

(The *BABAR* Collaboration)

[1] *Laboratoire d'Annecy-le-Vieux de Physique des Particules (LAPP), Université de Savoie, CNRS/IN2P3, F-74941 Annecy-Le-Vieux, France*
[2] *Universitat de Barcelona, Facultat de Fisica, Departament ECM, E-08028 Barcelona, Spain*
[3] *INFN Sezione di Bari[a]; Dipartimento to di Fisica, Università di Bari[b], I-70126 Bari, Italy*
[4] *University of Bergen, Institute of Physics, N-5007 Bergen, Norway*
[5] *Lawrence Berkeley National Laboratory and University of California, Berkeley, California 94720, USA*
[6] *University of Birmingham, Birmingham, B15 2TT, United Kingdom*
[7] *Ruhr Universität Bochum, Institut für Experimentalphysik 1, D-44780 Bochum, Germany*
[8] *University of British Columbia, Vancouver, British Columbia, Canada V6T 1Z1*
[9] *Brunel University, Uxbridge, Middlesex UB8 3PH, United Kingdom*
[10] *Budker Institute of Nuclear Physics, Novosibirsk 630090, Russia*
[11] *University of California at Irvine, Irvine, California 92697, USA*
[12] *University of California at Riverside, Riverside, California 92521, USA*
[13] *University of California at Santa Barbara, Santa Barbara, California 93106, USA*
[14] *University of California at Santa Cruz, Institute for Particle Physics, Santa Cruz, California 95064, USA*
[15] *California Institute of Technology, Pasadena, California 91125, USA*
[16] *University of Cincinnati, Cincinnati, Ohio 45221, USA*
[17] *University of Colorado, Boulder, Colorado 80309, USA*
[18] *Colorado State University, Fort Collins, Colorado 80523, USA*
[19] *Technische Universität Dortmund, Fakultät Physik, D-44221 Dortmund, Germany*
[20] *Technische Universität Dresden, Institut für Kern- und Teilchenphysik, D-01062 Dresden, Germany*
[21] *Laboratoire Leprince-Ringuet, CNRS/IN2P3, Ecole Polytechnique, F-91128 Palaiseau, France*
[22] *University of Edinburgh, Edinburgh EH9 3JZ, United Kingdom*
[23] *INFN Sezione di Ferrara[a]; Dipartimento di Fisica, Università di Ferrara[b], I-44100 Ferrara, Italy*
[24] *INFN Laboratori Nazionali di Frascati, I-00044 Frascati, Italy*
[25] *INFN Sezione di Genova[a]; Dipartimento di Fisica, Università di Genova[b], I-16146 Genova, Italy*
[26] *Indian Institute of Technology Guwahati, Guwahati, Assam, 781 039, India*
[27] *Harvard University, Cambridge, Massachusetts 02138, USA*
[28] *Universität Heidelberg, Physikalisches Institut, Philosophenweg 12, D-69120 Heidelberg, Germany*
[29] *Humboldt-Universität zu Berlin, Institut für Physik, Newtonstr. 15, D-12489 Berlin, Germany*
[30] *Imperial College London, London, SW7 2AZ, United Kingdom*
[31] *University of Iowa, Iowa City, Iowa 52242, USA*
[32] *Iowa State University, Ames, Iowa 50011-3160, USA*
[33] *Johns Hopkins University, Baltimore, Maryland 21218, USA*
[34] *Laboratoire de l'Accélérateur Linéaire, IN2P3/CNRS et Université Paris-Sud 11, Centre Scientifique d'Orsay, B. P. 34, F-91898 Orsay Cedex, France*
[35] *Lawrence Livermore National Laboratory, Livermore, California 94550, USA*
[36] *University of Liverpool, Liverpool L69 7ZE, United Kingdom*
[37] *Queen Mary, University of London, London, E1 4NS, United Kingdom*
[38] *University of London, Royal Holloway and Bedford New College, Egham, Surrey TW20 0EX, United Kingdom*
[39] *University of Louisville, Louisville, Kentucky 40292, USA*
[40] *Johannes Gutenberg-Universität Mainz, Institut für Kernphysik, D-55099 Mainz, Germany*
[41] *University of Manchester, Manchester M13 9PL, United Kingdom*
[42] *University of Maryland, College Park, Maryland 20742, USA*

[43]University of Massachusetts, Amherst, Massachusetts 01003, USA
[44]Massachusetts Institute of Technology, Laboratory for Nuclear Science, Cambridge, Massachusetts 02139, USA
[45]McGill University, Montréal, Québec, Canada H3A 2T8
[46]INFN Sezione di Milano[a]; Dipartimento di Fisica, Università di Milano[b], I-20133 Milano, Italy
[47]University of Mississippi, University, Mississippi 38677, USA
[48]Université de Montréal, Physique des Particules, Montréal, Québec, Canada H3C 3J7
[49]INFN Sezione di Napoli[a]; Dipartimento di Scienze Fisiche,
Università di Napoli Federico II[b], I-80126 Napoli, Italy
[50]NIKHEF, National Institute for Nuclear Physics and High Energy Physics, NL-1009 DB Amsterdam, The Netherlands
[51]University of Notre Dame, Notre Dame, Indiana 46556, USA
[52]Ohio State University, Columbus, Ohio 43210, USA
[53]University of Oregon, Eugene, Oregon 97403, USA
[54]INFN Sezione di Padova[a]; Dipartimento di Fisica, Università di Padova[b], I-35131 Padova, Italy
[55]Laboratoire de Physique Nucléaire et de Hautes Energies,
IN2P3/CNRS, Université Pierre et Marie Curie-Paris6,
Université Denis Diderot-Paris7, F-75252 Paris, France
[56]INFN Sezione di Perugia[a]; Dipartimento di Fisica, Università di Perugia[b], I-06100 Perugia, Italy
[57]INFN Sezione di Pisa[a]; Dipartimento di Fisica,
Università di Pisa[b]; Scuola Normale Superiore di Pisa[c], I-56127 Pisa, Italy
[58]Princeton University, Princeton, New Jersey 08544, USA
[59]INFN Sezione di Roma[a]; Dipartimento di Fisica,
Università di Roma La Sapienza[b], I-00185 Roma, Italy
[60]Universität Rostock, D-18051 Rostock, Germany
[61]Rutherford Appleton Laboratory, Chilton, Didcot, Oxon, OX11 0QX, United Kingdom
[62]CEA, Irfu, SPP, Centre de Saclay, F-91191 Gif-sur-Yvette, France
[63]SLAC National Accelerator Laboratory, Stanford, California 94309 USA
[64]University of South Carolina, Columbia, South Carolina 29208, USA
[65]Southern Methodist University, Dallas, Texas 75275, USA
[66]Stanford University, Stanford, California 94305-4060, USA
[67]State University of New York, Albany, New York 12222, USA
[68]Tel Aviv University, School of Physics and Astronomy, Tel Aviv, 69978, Israel
[69]University of Tennessee, Knoxville, Tennessee 37996, USA
[70]University of Texas at Austin, Austin, Texas 78712, USA
[71]University of Texas at Dallas, Richardson, Texas 75083, USA
[72]INFN Sezione di Torino[a]; Dipartimento di Fisica Sperimentale, Università di Torino[b], I-10125 Torino, Italy
[73]INFN Sezione di Trieste[a]; Dipartimento di Fisica, Università di Trieste[b], I-34127 Trieste, Italy
[74]IFIC, Universitat de Valencia-CSIC, E-46071 Valencia, Spain
[75]University of Victoria, Victoria, British Columbia, Canada V8W 3P6
[76]Department of Physics, University of Warwick, Coventry CV4 7AL, United Kingdom
[77]University of Wisconsin, Madison, Wisconsin 53706, USA

(Dated: June 23, 2010)

We report results from an updated study of the suppressed decays $B^- \to DK^-$ and $B^- \to D^*K^-$ followed by $D \to K^+\pi^-$, where $D^{(*)}$ indicates a $D^{(*)0}$ or a $\bar{D}^{(*)0}$ meson, and $D^* \to D\pi^0$ or $D^* \to D\gamma$. These decays are sensitive to the CKM unitarity triangle angle γ due to interference between the $b \to c$ transition $B^- \to D^{(*)0}K^-$ followed by the doubly Cabibbo-suppressed decay $D^0 \to K^+\pi^-$, and the $b \to u$ transition $B^- \to \bar{D}^{(*)0}K^-$ followed by the Cabibbo-favored decay $\overline{D}^0 \to K^+\pi^-$. We also report an analysis of the decay $B^- \to D^{(*)}\pi^-$ with the D decaying into the doubly Cabibbo-suppressed mode $D \to K^+\pi^-$. Our results are based on 467 million $\Upsilon(4S) \to B\overline{B}$ decays collected with the *BABAR* detector at SLAC. We measure the ratios $\mathcal{R}^{(*)}$ of the suppressed ($[K^+\pi^-]_D K^-/\pi^-$) to favored ($[K^-\pi^+]_D K^-/\pi^-$) branching fractions as well as the *CP* asymmetries $\mathcal{A}^{(*)}$ of those modes. We see indications of signals for the $B^- \to DK^-$ and $B^- \to D^*_{D\pi^0}K^-$ suppressed modes, with statistical significances of 2.1 and 2.2σ, respectively, and we measure:

$$\mathcal{R}_{DK} = (1.1 \pm 0.6 \pm 0.2) \times 10^{-2},\ \mathcal{A}_{DK} = -0.86 \pm 0.47\ ^{+0.12}_{-0.16},$$

$$\mathcal{R}^*_{(D\pi^0)K} = (1.8 \pm 0.9 \pm 0.4) \times 10^{-2},\ \mathcal{A}^*_{(D\pi^0)K} = +0.77 \pm 0.35 \pm 0.12,$$

$$\mathcal{R}^*_{(D\gamma)K} = (1.3 \pm 1.4 \pm 0.8) \times 10^{-2},\ \mathcal{A}^*_{(D\gamma)K} = +0.36 \pm 0.94\ ^{+0.25}_{-0.41},$$

where the first uncertainty is statistical and the second is systematic. We use a frequentist approach to obtain the magnitude of the ratio $r_B \equiv |A(B^- \to \overline{D}^0K^-)/A(B^- \to D^0K^-)| = (9.5^{+5.1}_{-4.1})\%$, with $r_B < 16.7\%$ at 90% confidence level. In the case of $B^- \to D^*K^-$ we find $r^*_B \equiv |A(B^- \to \overline{D}^{*0}K^-)/A(B^- \to D^{*0}K^-)| = (9.6^{+3.5}_{-5.1})\%$, with $r^*_B < 15.0\%$ at 90% confidence level.

PACS numbers: 13.25.Hw, 14.40.Nd, 12.15.Hh, 11.30.Er

I. INTRODUCTION

The Standard Model accommodates *CP* violation through a single phase in the Cabibbo-Kobayashi-Maskawa (CKM) quark mixing matrix V [1]. In the Wolfenstein parameterization [2], the angle $\gamma = \arg\left(-V_{ud}V_{ub}^{*}/V_{cd}V_{cb}^{*}\right)$ of the unitarity triangle is related to the complex phase of the CKM matrix element V_{ub} through $V_{ub} = |V_{ub}|e^{-i\gamma}$. A theoretically clean source of information on the angle γ is provided by $B^- \to D^{(*)} K^-$ decays, where $D^{(*)}$ represents an admixture of $D^{(*)0}$ and $\overline{D}^{(*)0}$ states. These decays exploit the interference between $B^- \to D^{(*)0}K^-$ and $B^- \to \overline{D}^{(*)0}K^-$ (Fig. 1) that occurs when the $D^{(*)0}$ and the $\overline{D}^{(*)0}$ decay to common final states.

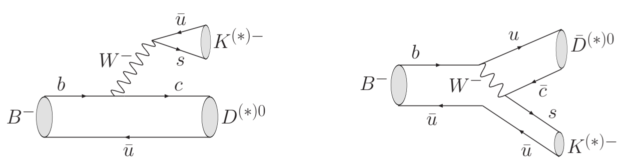

FIG. 1: Feynman diagrams for $B^- \to D^{(*)0}K^{(*)-}$ and $\overline{D}^{(*)0}K^{(*)-}$. The latter is CKM and color-suppressed with respect to the former.

In the Atwood-Dunietz-Soni (ADS) method [3], the D^0 from the favored $\to c$ amplitude is reconstructed in the doubly Cabibbo-suppressed decay $K^+\pi^-$, while the $\overline{D}^0$ from the $\to u$ suppressed amplitude is reconstructed in the favored decay $K^+\pi^-$. The product branching fractions for these final states, which we denote as $[K^+\pi^-]_D K^-$ ($B^- \to DK^-$) and $[K^+\pi^-]_{D^*}K^-$ ($B^- \to D^*K^-$), are small ($\sim 10^{-7}$), but the two interfering amplitudes are of the same order of magnitude, and large *CP* asymmetries are therefore possible. The favored decay mode $B^- \to [K^-\pi^+]_{D^{(*)}}K^-$ is used to normalize the measurement and cancel many systematic uncertainties. Thus, ignoring possible small effects due to D mixing and assuming no *CP* violation in the normalization modes, we define the charge-specific ratios for B^+ and B^- decay rates to the ADS final states as

$$\begin{aligned}\mathcal{R}_{DK}^{\pm} &\equiv \frac{\Gamma([K^{\mp}\pi^{\pm}]_D K^{\pm})}{\Gamma([K^{\pm}\pi^{\mp}]_D K^{\pm})} \\ &= r_B^2 + r_D^2 + 2\, r_B r_D \cos(\pm\gamma + \delta), \end{aligned} \tag{1}$$

where $r_B = |A(B^- \to \overline{D}^0K^-)/A(B^- \to D^0K^-)| \approx 10\%$ [4–7] and $r_D = |A(D^0 \to K^+\pi^-)/A(D^0 \to K^-\pi^+)| = (5.78 \pm 0.08)\%$ [8] are the suppressed to favored B and D amplitude ratios. The rates in Eq. (1) depend on the relative weak phase γ and the relative strong phase $\delta \equiv \delta_B + \delta_D$ between the interfering amplitudes, where δ_B and δ_D are the strong phase differences between the two B and D decay amplitudes, respectively. The value of δ_D has been measured to be $\delta_D = (201.9^{+11.3}_{-12.4})^\circ$ [8], where we have accounted for a phase shift of 180° in the definition of δ_D between Ref. [8] and this analysis.

The main experimental observables are the charge-averaged decay rate and the direct *CP* asymmetry, which can be written as

$$\begin{aligned}\mathcal{R}_{DK} &\equiv \frac{1}{2}\left(\mathcal{R}_{DK}^{+} + \mathcal{R}_{DK}^{-}\right) \\ &= r_B^2 + r_D^2 + 2\, r_B r_D \cos\gamma\cos\delta \end{aligned} \tag{2}$$

$$\begin{aligned}\mathcal{A}_{DK} &\equiv \frac{\mathcal{R}_{DK}^{-} - \mathcal{R}_{DK}^{+}}{\mathcal{R}_{DK}^{-} + \mathcal{R}_{DK}^{+}} \\ &= 2\, r_B r_D \sin\gamma\sin\delta/\mathcal{R}_{DK}. \end{aligned} \tag{3}$$

The treatment for the D^*K mode is identical to the DK one, but the parameters r_B^* and δ_B^* are not expected to be numerically the same as those of the DK mode. Taking into account the effective strong phase difference of π between the D^* decays to $D\gamma$ and $D\pi^0$[9], we define the charge-specific ratios for D^* as:

$$\begin{aligned}\mathcal{R}_{(D\pi^0)K}^{*\pm} &\equiv \frac{\Gamma([K^{\mp}\pi^{\pm}]_{D^*\to D\pi^0}K^{\pm})}{\Gamma([K^{\pm}\pi^{\mp}]_{D^*\to D\pi^0}K^{\pm})} \\ &= r_B^{*2} + r_D^2 + 2\, r_B^* r_D \cos(\pm\gamma + \delta^*), \end{aligned} \tag{4}$$

$$\begin{aligned}\mathcal{R}_{(D\gamma)K}^{*\pm} &\equiv \frac{\Gamma([K^{\mp}\pi^{\pm}]_{D^*\to D\gamma}K^{\pm})}{\Gamma([K^{\pm}\pi^{\mp}]_{D^*\to D\gamma}K^{\pm})} \\ &= r_B^{*2} + r_D^2 - 2\, r_B^* r_D \cos(\pm\gamma + \delta^*), \end{aligned} \tag{5}$$

with $r_B^* = |A(B^- \to \bar{D}^{*0}K^-)/A(B^- \to D^{*0}K^-)|$ and $\delta^* \equiv \delta_B^* + \delta_D$, where δ_B^* is the strong phase difference between the two B decay amplitudes. The charge averaged ratios for $D^* \to D\pi^0$ and $D^* \to D\gamma$ are then:

$$\begin{aligned}\mathcal{R}_{(D\pi^0)K}^{*} &\equiv \frac{1}{2}\left(\mathcal{R}_{(D\pi^0)K}^{*+} + \mathcal{R}_{(D\pi^0)K}^{*-}\right) \\ &= r_B^{*2} + r_D^2 + 2\, r_B^* r_D \cos\gamma\cos\delta^*, \end{aligned} \tag{6}$$

$$\begin{aligned}\mathcal{R}_{(D\gamma)K}^{*} &\equiv \frac{1}{2}\left(\mathcal{R}_{(D\gamma)K}^{*+} + \mathcal{R}_{(D\gamma)K}^{*-}\right) \\ &= r_B^{*2} + r_D^2 - 2\, r_B^* r_D \cos\gamma\cos\delta^*. \end{aligned} \tag{7}$$

---

*Now at Temple University, Philadelphia, Pennsylvania 19122, USA
†Also with Università di Perugia, Dipartimento di Fisica, Perugia, Italy
‡Also with Università di Roma La Sapienza, I-00185 Roma, Italy
§Now at University of South Alabama, Mobile, Alabama 36688, USA
¶Also with Università di Sassari, Sassari, Italy

Definitions of the direct *CP* asymmetries $\mathcal{A}^*_{(D\pi^0)K}$ and $\mathcal{A}^*_{(D\gamma)K}$ follow Eq. (3).

This paper is an update of our previous ADS analysis in Ref. [4], which used $232 \times 10^6 B\overline{B}$ pairs and set 90% C.L. upper limits $\mathcal{R}_{DK} < 0.029$, $\mathcal{R}^*_{(D\pi^0)K} < 0.023$ and $\mathcal{R}^*_{(D\gamma)K} < 0.045$. In addition to an increased data sample, new features in the analysis include a multi-dimensional fit involving the neural network output used to discriminate the signal from the continuum background, rather than a simple cut on this variable as was done in the previous analysis. We also include measurements of the ratios of the doubly Cabibbo-suppressed to Cabibbo-favored $D^{(*)}\pi$ decay rates,

$$\mathcal{R}^{(*)\pm}_{D\pi} \equiv \frac{\Gamma(B^\pm \to [K^\mp\pi^\pm]_{D^{(*)}}\pi^\pm)}{\Gamma(B^\pm \to [K^\pm\pi^\mp]_{D^{(*)}}\pi^\pm)}, \quad (8)$$

and of the corresponding asymmetries. These measurements are used as a check for the $B^- \to [K^+\pi^-]_{D^{(*)}}K^-$ ADS analysis. In the $D^{(*)}\pi$ case, we expect that the ratio $r_B^{(*)(D\pi)}$ of the V_{ub} to V_{cb} amplitudes is suppressed by a factor $|V_{cd}V_{us}/V_{ud}V_{cs}|$ compared to the $D^{(*)}K$ case, if we assume the same color suppression factor for both decays. One expects therefore $r_B^{(*)(D\pi)} \approx r_B^{(*)} \times \tan^2\theta_c \approx 5 \times 10^{-3} \ll r_D$, where θ_c is the Cabibbo angle and where we have assumed $r_B^{(*)} = 10\%$. Neglecting higher order terms, $\mathcal{R}^{(*)}_{D\pi} \simeq r_D^2$ and $\mathcal{A}^{(*)}_{D\pi} \simeq 2r_B^{(*)}\tan^2\theta_c \sin\gamma\sin\delta^{(*)}/r_D$. Hence, the maximum asymmetry possible for $D^{(*)}\pi$ ADS decays is $2r_B^{(*)}\tan^2\theta_c/r_D \approx 18\%$.

II. THE *BABAR* DETECTOR AND DATASET

The results presented in this paper are based on $467\times10^6\ \Upsilon(4S) \to B\overline{B}$ decays, corresponding to an integrated luminosity of 426 fb^{-1} (on-peak data). The data were collected between 1999 and 2007 with the *BABAR* detector [10] at the PEP-II e^+e^- collider at SLAC. In addition, a 44 fb^{-1} data sample, with center-of-mass (CM) energy 40 MeV below the $\Upsilon(4S)$ resonance (off-peak data), is used to study backgrounds from continuum events, $e^+e^- \to q\bar{q}$ ($q = u, d, s$, or c).

The *BABAR* detector response to various physics processes as well as to varying beam and environmental conditions is modeled with simulation software based on the `Geant4` [11] tool kit. We use `EVTGEN` [12] to model the kinematics of B meson decays and `JETSET` [13] to model continuum processes $e^+e^- \to q\bar{q}$.

III. ANALYSIS METHOD

A. Basic Requirements

We reconstruct $B^- \to D^{(*)}K^-$ and $B^- \to D^{(*)}\pi^-$ with the D decaying to $K^-\pi^+$ (right-sign (RS) decays) and $K^+\pi^-$ (wrong-sign (WS) decays). For decays involving a D^*, both $D^* \to D\pi^0$ and $D^* \to D\gamma$ modes are reconstructed. Charged kaon and pion candidates must satisfy identification criteria that are typically 85% efficient, depending on momentum and polar angle. The misidentification rates are at the few percent level. We select D candidates with an invariant mass within $20\,\mathrm{MeV}/c^2$ (about 3 standard deviations) of the known D^0 mass [14]. All D candidates are mass and vertex constrained. For modes with $D^* \to D\pi^0$ or $D^* \to D\gamma$, the mass difference Δm between the D^* and the D must be within $4\,\mathrm{MeV}/c^2$ ($\simeq 4\sigma$) or $15\,\mathrm{MeV}/c^2$ ($\simeq 2\sigma$), respectively, of the nominal mass difference [14].

For the WS decays $B^\pm \to [K^\mp\pi^\pm]_D K^\pm$, two important sources of background arise: the first from $B^\pm \to [\pi^\mp K^\pm]_D K^\pm$ (in which the K and π in the D decay are misidentified as π and K) and the second from $B^\pm \to [K^\mp K^\pm]_D \pi^\pm$ (when the $K^\mp$ $\pi^\pm$ pair has an invariant mass within $20\,\mathrm{MeV}/c^2$ of the nominal D^0 mass). To eliminate the first background, we recompute the invariant mass (M_{switch}) of the $h^+h'^-$ pair in $D^0 \to h^+h'^-$ switching the mass assumptions on the h^+ and the h'^-. We veto candidates with M_{switch} within $20\,\mathrm{MeV}/c^2$ of the D^0 mass [14]. To eliminate the second background, we also veto any candidate where the KK invariant mass is within $20\,\mathrm{MeV}/c^2$ of the D^0 mass. To ensure the same selection efficiencies, these criteria are applied both to $B^\pm \to [K^\mp\pi^\pm]_{D^{(*)}}K^\pm$ and to $B^\pm \to [K^\pm\pi^\mp]_{D^{(*)}}K^\pm$ candidates. These veto cuts are 88% efficient on signal decays.

We identify B candidates using two nearly independent kinematic variables that are customarily used when reconstructing B-meson decays at the $\Upsilon(4S)$. These variables are the energy-substituted mass, $m_{\mathrm{ES}} \equiv \sqrt{(\frac{s}{2} + \vec{p}_0\cdot\vec{p}_B)^2/E_0^2 - p_B^2}$ and energy difference $\Delta E \equiv E_B^* - \frac{1}{2}\sqrt{s}$, where E and p are energy and momentum, the asterisk denotes the CM frame, the subscripts 0 and B refer to the $\Upsilon(4S)$ and B candidate, respectively, and s is the square of the CM energy. For signal events $m_{\mathrm{ES}} = m_{B^+}$ [14] and $\Delta E = 0$ within the resolutions of about 2.6 MeV/c^2 and 17 MeV, respectively. We require that all candidates have $|\Delta E| < 40\,\mathrm{MeV}$ and we use m_{ES} in the fit to extract the number of signal events.

The average number of $B \to D^{(*)}K$ candidates reconstructed per selected event is about 1.4 in $B \to DK$ signal Monte Carlo (MC) events and about 2 for $B \to D^*K$ signal MC events. This is mostly due to the cross-feed between the DK and the D^*K final states. For all events with multiple $B \to D^{(*)}K$ candidates, we retain only one candidate per event, based on the smallest value of $|\Delta E|$. This method does not bias the sample since ΔE is not used to extract the number of signal events. After this arbitration, less than 0.4% (0.5%) of the $B \to DK$ ($B \to D^*K$) signal MC events selected are reconstructed as $B \to D^*K$ ($B \to DK$). About 10% of the $B \to D^*_{D\pi^0}K$ events selected are reconstructed as $B \to D^*_{D\gamma}K$ and about 2% of the $B \to D^*_{D\gamma}K$ events selected are reconstructed as $B \to D^*_{D\pi^0}K$.

TABLE I: Selection efficiencies, after correction for known data/MC differences, for $B^{\mp} \to [K^{\pm}\pi^{\mp}]_{D^{(*)}} h^{\mp}$ (ϵ_{WS}) and $B^{\mp} \to [K^{\mp}\pi^{\pm}]_{D^{(*)}} h^{\mp}$ (ϵ_{RS}), and efficiency ratio $\epsilon_{WS}/\epsilon_{RS}$.

Channel	ϵ_{WS} (%)	ϵ_{RS} (%)	$\epsilon_{WS}/\epsilon_{RS}$ (10^{-2})
DK	26.5±0.1	26.6±0.1	99.6±0.5
$D^*_{D\pi^0}K$	13.3±0.1	13.2±0.1	100.6±1.1
$D^*_{D\gamma}K$	17.4±0.1	17.5±0.1	99.8±0.8
$D\pi$	26.0±0.1	26.5±0.1	97.9±0.5
$D^*_{D\pi^0}\pi$	14.3±0.1	14.8±0.1	96.4±0.9
$D^*_{D\gamma}\pi$	18.8±0.1	19.5±0.1	96.3±0.7

The $B \to D^{(*)}\pi$ analysis is performed independently of the $B \to D^{(*)}K$ analysis, but uses the same multiple candidate selection algorithm. A summary of the selection efficiencies for the WS modes $[K^{\pm}\pi^{\mp}]_{D^{(*)}} h^{\mp}$ (h=K,π) and the RS modes $[\pi^{\pm}K^{\mp}]_{D^{(*)}} h^{\mp}$ is given in Table I.

B. Neural Network

After these initial requirements, backgrounds dominantly arise from continuum events, especially $e^+e^- \to c\bar{c}$, with $\bar{c} \to \overline{D}^0X$, $\overline{D}^0 \to K^+\pi^-$ and $c \to D^0X$, $D^0 \to K^-$+anything. The continuum background is reduced by using neural network techniques. To select the discriminating variables used in the neural network, we rely on a study performed for the previous version of this analysis [4], and we consider the seven quantities listed below:

1. Two event shape moments $L_0 = \sum_i p_i$, and $L_2 = \sum_i p_i \cos^2\theta_i$, calculated in the CM frame. Here, p_i is the momentum and θ_i is the angle with respect to the thrust axis of the B candidate; the index i runs over all tracks and clusters not used to reconstruct the B meson (rest of the event). These variables are sensitive to the shape of the event, separating jet-like continuum events from more spherical $B\overline{B}$ events.

2. The absolute value of the cosine of the angle in the CM frame between the thrust axes of the B candidate and the detected remainder of the event, $|\cos\theta_T|$. The distribution of $|\cos\theta_T|$ is approximately uniform for signal and strongly peaked at one for continuum background.

3. The absolute value of the cosine of the CM angle between the B candidate momentum and the beam axis, $|\cos\theta_B|$. In this variable, the signal follows a $1-\cos^2\theta_B$ distribution, while the background is approximately uniform.

4. The charge difference ΔQ between the sum of the charges of tracks in the $D^{(*)}$ hemisphere and the sum of the charges of the tracks in the opposite hemisphere, excluding the tracks used in the reconstructed B, and where the partitioning of the event into two hemispheres is done in the CM frame. This variable exploits the correlation occurring in $c\bar{c}$ events between the charge of the c (or $\bar{c}$) in a given hemisphere and the sum of the charges of all particles in that hemisphere. For signal events, the average charge difference is $\langle\Delta Q\rangle = 0$, whereas for the $c\bar{c}$ background $\langle\Delta Q\rangle \approx \frac{7}{3} \times Q_B$, where Q_B is the charge of the B candidate.

5. The product $Q_B \cdot Q_K$, where Q_K is the sum of the charges of all kaons in the rest of the event. In many signal events, there is a charged kaon among the decay products of the other B in the event. The charge of this kaon tends to be highly correlated with the charge of the B. Thus, signal events tend to have $Q_B \cdot Q_K \leq -1$. On the other hand, most continuum events have no kaons outside of the reconstructed B, and therefore $Q_K = 0$.

6. A quantity $\mathcal{M}_{K\ell}$, defined to be zero if there are no leptons (e or μ) in the event, and, if a lepton is found, taken to be equal to the invariant mass of this lepton and the kaon from B (bachelor K). This quantity differentiates between continuum background and signal because continuum events have fewer leptons than $B\overline{B}$ events. Furthermore, a large fraction of leptons in $c\bar{c}$ background events are from $D \to K\ell\nu$, where the kaon becomes the bachelor kaon candidate, so that the average $\mathcal{M}_{K\ell}$ in $c\bar{c}$ events is lower than in B signal events.

7. The absolute value of the measured proper time interval between the two B decays, $|\Delta t|$. This is calculated from the measured separation, Δz, between the decay points of the reconstructed B and the other B along the beam direction, and the known Lorentz boost of the initial e^+e^- state. For continuum background, $|\Delta t|$ is peaked at 0, with most events having $|\Delta t| < 2\,\text{ps}$, while it is less peaked and can extend beyond $5\,\text{ps}$ for $B^{\pm} \to D^{(*)}h^{\pm}$ signal events.

The neural network is trained with simulated continuum and signal $[K^{\pm}\pi^{\mp}]_{D^{(*)}} K^{\mp}$ events. Only wrong-sign $D^{(*)}K$ candidates are used in the training, but the neural network is used in the analysis of all the $D^{(*)}h^{\mp}$ channels. The distributions of the neural network output (NN) for signal-enriched right-sign control samples are compared with expectations from the MC simulation in Fig. 2(a) (DK) and Fig. 2(d) ($D\pi$). The agreement is satisfactory. In the same figure, the NN spectra of background control samples (off-peak data) are compared with expectations from continuum $q\bar{q}$ MC. Since we do not expect these distributions to be exactly the same for the right-sign and wrong-sign background samples, they are shown separately for the $[K^{\pm}\pi^{\mp}]_{D^{(*)}} K^{\mp}$(Fig. 2(b)), $[K^{\mp}\pi^{\pm}]_{D^{(*)}} K^{\mp}$ (Fig. 2(c)), $[K^{\pm}\pi^{\mp}]_{D^{(*)}} \pi^{\mp}$(Fig. 2(e)) and $[K^{\mp}\pi^{\pm}]_{D^{(*)}} \pi^{\mp}$ (Fig. 2(f)) channels. To increase the statistics, the m_{ES}

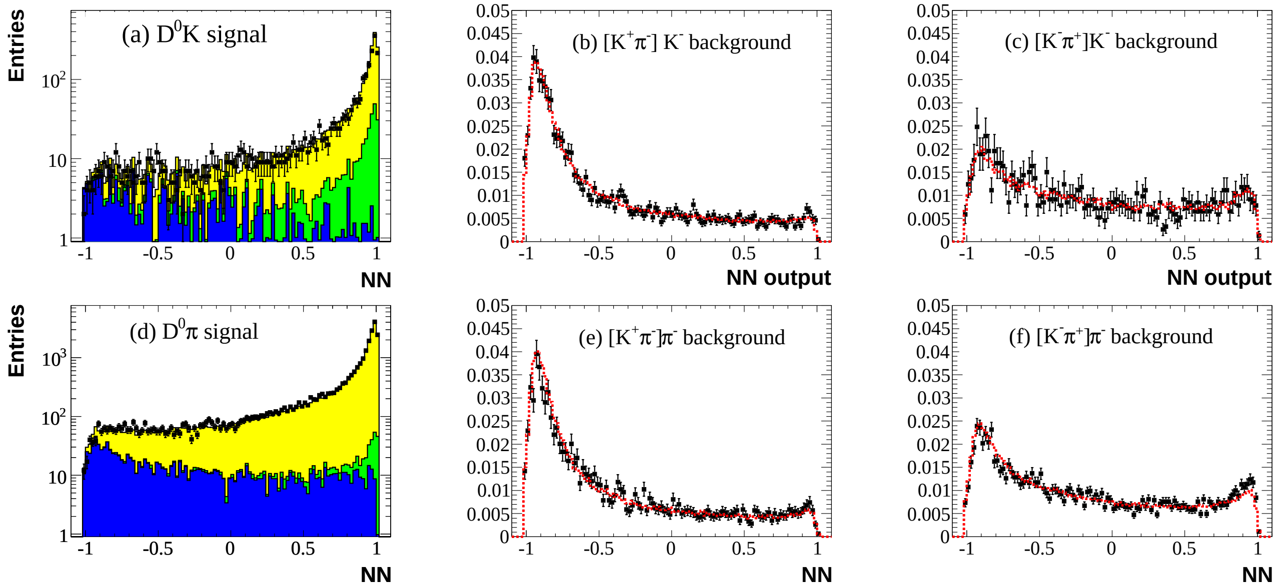

FIG. 2: (color online). Signal and background distributions of the neural network output, and results of the NN verifications for DK (a), $D^{(*)}K$ (b, c), $D\pi$ (d) and $D^{(*)}\pi$ (e, f) candidates. (a,d): $Dh^{\pm}$ right-sign candidates, signal-enriched by a cut on the ΔE, $m_{\rm ES}$ signal region. Shaded plain histograms are MC expectations for $q\bar{q}$ background (dark gray/blue), $b\bar{b}$ background (middle gray/green) and $B^{\pm} \to Dh^{\pm}$ signal events (light gray/yellow). Points with error bars are on-peak data. (b,e): $D^{(*)}h^{\pm}$ wrong-sign background. (c,f): $D^{(*)}h^{\pm}$ right-sign background. Plots b, c, e, and f are normalized to unity. The dotted line histograms show the distribution of simulated continuum events. The off-peak data used to check the NN are overlaid as data points. To increase the statistics, the $m_{\rm ES}$ and ΔE requirements on the off-peak and continuum MC events have been relaxed, and $Dh^{\pm}$ and $D^{*}h^{\pm}$ contributions have been summed.

and ΔE requirements on the off-resonance and continuum MC events have been relaxed, and the $Dh^{\pm}$ and $D^{*}h^{\pm}$ contributions have been summed, after checking that they are in agreement with each other. Good agreement between data and the simulation is observed in all channels. Good agreement between the $D^{(*)}K$ and the $D^{(*)}\pi$ background NN distributions is also visible in Fig. 2, while on the contrary the background NN distribution of wrong-sign decays is clearly different from the background NN distribution of right-sign decays. We have examined the distributions of all variables used in the neural network, and found good agreement between the simulation and the data control samples. Finally, we examined the NN distributions in the signal MC for the different B signal channels, right-sign and wrong-sign separately ($D\pi$, $D^{*}\pi$, DK, $D^{*}K$) and did not observe any significant difference between these channels.

C. Fitting for event yields and $\mathcal{R}^{(*)}$

The ratios $\mathcal{R}^{(*)}$ are extracted by performing extended unbinned maximum likelihood fits to the set of variables $m_{\rm ES}$, NN, and $I_{\rm sign}$, where $I_{\rm sign}$ is a discrete variable equal to 0 for WS events and to 1 for RS events. We write the extended likelihood $\mathcal{L}$ as

$$\mathcal{L} = \frac{e^{-N'}}{N!} N'^{N} \prod_{j=1}^{N} f(\mathbf{x}_j|\theta),$$

where the vector $\mathbf{x}$ indicates the variables ($m_{\rm ES}$, NN, and $I_{\rm sign}$) and θ indicates the set of parameters which are fitted from the data. N is the total number of signal and background events, and $N' = \sum_i N_i$ is the expectation value for the total number of events. The sum runs over the different signal and background categories i which will be detailed below. The probability density function (PDF) $f(\mathbf{x}_j|\theta)$ is written as the sum over the different signal and background categories

$$f(\mathbf{x}_j|\theta, N') = \frac{\sum_i N_i f_i(\mathbf{x}_j|\theta)}{N'},$$

where $f_i(\mathbf{x}|\theta)$ is the product $F(m_{\rm ES}) \times G(NN) \times H(I_{\rm sign})$ of an $m_{\rm ES}$ component $F(m_{\rm ES})$, a NN component $G(NN)$ and a two-bin histogram $H(I_{\rm sign})$ set to (1,0) for the WS category and (0,1) for the RS category. The NN distributions are all modeled by histograms with 102 bins between -1.02 and 1.02.

The fits are performed separately to each of the $D\pi$, $D^{*}_{D\pi^0}\pi$, $D^{*}_{D\gamma}\pi$, DK, $D^{*}_{D\pi^0}K$ and $D^{*}_{D\gamma}K$ samples. They are configured in such a way that $\mathcal{R}^{(*)}$ is an explicit fit parameter: for the B signal, we fit for the number of right-sign decays N_{RS} and the ratio $\mathcal{R}^{(*)} = N_{WS}/(c \times N_{RS})$, where N_{WS} is the number of wrong-sign signal events and c is the ratio of the wrong-sign to right-sign selection efficiencies. For $B \to D^{(*)}K$, the factor c is consistent with unity within the statistical precision of the simulation (Table I) and is set to this value in the fits. For $B \to D^{(*)}\pi$, c differs slightly from unity due to different particle identification cuts applied at an early stage of the event selection and we use therefore the values of Table I in the fits.

The following signal and background categories are used to describe each sample in the fits:

1. The right-sign signal $B^- \to [K^-\pi^+]_{D^{(*)}}K^-/\pi^-$: its $m_{\rm ES}$ spectrum is modeled by a Gaussian function $\mathcal{G}_{sig}(m_{\rm ES})$ whose mean and width are determined from the fit to data. The NN PDF $\mathcal{NN}_{sig}$ is constructed from the NN spectrum of the $B^- \to Dh^-$ signal MC.

2. The wrong-sign signal $B^- \to [K^+\pi^-]_{D^{(*)}}K^-/\pi^-$: its $m_{\rm ES}$ and NN spectra have the same parametrizations $\mathcal{G}_{sig}(m_{\rm ES})$ and $\mathcal{NN}_{sig}$ as the right-sign signal.

3. The right-sign combinatorial background from $q\bar{q}$ ($q = u, d, s, c$) events into $[K^-\pi^+]K^-$ (DK) or $[K^-\pi^+]\pi^-$ ($D\pi$): its $m_{\rm ES}$ component is modeled with the ARGUS function [15] $\mathcal{A}_{q\bar{q}}(m_{\rm ES})$ whose shape and endpoint parameters, $\zeta_{q\bar{q}}$ and m_0, are allowed to vary in the fit. The NN PDF $\mathcal{NN}_{q\bar{q}}^{(RS)}$ is constructed from the NN spectrum of $[K^-\pi^+]K^-$ (DK) or $[K^-\pi^+]\pi^-$ ($D\pi$) candidates in the $q\bar{q}$ continuum MC (Figs. 2c and 2f), where the ΔE requirement has been extended to $|\Delta E| < 200\,\mathrm{MeV}$ and the DK and D^*K (or $D\pi$ and $D^*\pi$) samples have been summed to increase the statistics.

4. The wrong-sign combinatorial background from $q\bar{q}$ events into $[K^+\pi^-]K^-$ (DK) or $[K^+\pi^-]\pi^-$ ($D\pi$): its $m_{\rm ES}$ component is parameterized by the same ARGUS function $\mathcal{A}_{q\bar{q}}(m_{\rm ES})$ used for the right-sign component. The NN PDF $\mathcal{NN}_{q\bar{q}}^{(WS)}$ is constructed from the NN spectrum of $[K^+\pi^-]K^-$ (DK) or $[K^+\pi^-]\pi^-$ ($D\pi$) candidates in the $q\bar{q}$ continuum MC (Figs. 2b and 2e).

5. The right-sign combinatorial background from $B\overline{B}$ events into $[K^-\pi^+]K^-$ (DK) or $[K^-\pi^+]\pi^-$ ($D\pi$), excluding the peaking background which is considered in category 7: its $m_{\rm ES}$ component is described by an ARGUS function [15] $\mathcal{A}_B^{(RS)}(m_{\rm ES})$ with shape parameter $\zeta_B^{(RS)}$ fixed to its value determined from $B\overline{B}$ MC, after removal of the $B \to D^{(*)}K/\pi$ signal events. The NN PDF used to describe this background is the PDF $\mathcal{NN}_{sig}$ describing the NN spectrum of the $B^- \to D^{(*)}h^-$ signal MC. The number of $B\overline{B}$ right-sign combinatorial background events is allowed to vary in the Dh^- fits but is fixed to the MC prediction in the D^*h^- fits (see below).

6. The wrong-sign combinatorial background from $B\overline{B}$ events into $[K^+\pi^-]K^-$ (DK) or $[K^+\pi^-]\pi^-$ ($D\pi$), excluding the peaking background which is considered in category 8: its $m_{\rm ES}$ component is described by an ARGUS function [15] $\mathcal{A}_B^{(WS)}(m_{\rm ES})$ with shape parameter $\zeta_B^{(WS)}$ fixed to its value determined from the $B\overline{B}$ MC, after removal of the $B \to D^{(*)}K/\pi$ signal events. The NN PDF used to describe this background is the PDF $\mathcal{NN}_{sig}$ describing the NN spectrum of the $B^- \to D^{(*)}h^-$ signal MC. The number of $B\overline{B}$ wrong-sign combinatorial background events is allowed to vary in the Dh^- fits but is fixed in the D^*h^- fits (see below).

7. The background from $B\overline{B}$ events in the right-sign component peaking in $m_{\rm ES}$ inside the signal region (peaking background): this background is discussed in more detail in Section IV. For the $DK^\pm$, $D\pi^\pm$ and $D^*_{D\pi^0}K^\pm$ categories, the peaking part of the $B\overline{B}$ background $m_{\rm ES}$ spectrum is described by the same Gaussian function $\mathcal{G}_{sig}(m_{\rm ES})$ as the signal. This component is therefore indistinguishable from the signal and its rate has to be fixed to the MC predictions. For the $D^*_{D\pi^0}\pi^\pm$, $D^*_{D\gamma}\pi^\pm$ and the $D^*_{D\gamma}K^\pm$ categories, the $m_{\rm ES}$ component is described by an asymmetric Gaussian whose shape parameters and amplitude for each category are determined from a fit to the $m_{\rm ES}$ spectrum of $B\overline{B}$ MC events, after vetoing the $B^\pm \to D^{(*)}h^\pm$ signal component. For all categories, the NN PDF used to describe this background is the PDF $\mathcal{NN}_{sig}$ describing the NN spectra of the $B \to D^{(*)}h^\pm$ signal MC.

8. The peaking background from $B\overline{B}$ events in the wrong-sign component: the treatment is similar to the previous component but $\mathcal{G}_{sig}(m_{\rm ES})$ is used to describe the $m_{\rm ES}$ spectrum of the $DK^\pm$, $D\pi^\pm$, $D^*_{D\pi^0}K^\pm$ and $D^*_{D\gamma}K^\pm$ categories, while an asymmetric Gaussian is used to describe the $m_{\rm ES}$ spectrum of the $D^*_{D\pi^0}\pi^\pm$ and $D^*_{D\gamma}\pi^\pm$ categories.

To summarize, we fit for the number of right-sign signal events N_{RS}, the ratio $\mathcal{R} = N_{WS}/(c \times N_{RS})$ of wrong-sign to right-sign events, the number of wrong-sign and right-sign $q\bar{q}$ combinatorial background events, $N_{WS}^{(q\bar{q})}$ and $N_{RS}^{(q\bar{q})}$, and for $Dh^\pm$ the number of wrong-sign and right-sign $B\overline{B}$ combinatorial background events, $N_{WS}^{(B\bar{B})}$ and $N_{RS}^{(B\bar{B})}$. We fix to their MC expectations the numbers of wrong-sign and right-sign $B\overline{B}$ peaking background, $N_{WS}^{(B\bar{B},pk)}$ and $N_{RS}^{(B\bar{B},pk)}$, as well as the number of $B\overline{B}$ combinatorial background events for $D^*h^\pm$. The other parameters fitted are the reconstructed $m_{\rm ES}$ peak and resolution, m_B and σ_{m_B}, and the $q\bar{q}$ continuum background shape parameter and endpoint, $\zeta_{q\bar{q}}$ and m_0.

TABLE II: Charmless background channels and branching fractions, $Dh^{\pm}$ channels affected by this background and background yields expected in our data sample.

Mode	Affected channel	$\mathcal{B}(10^{-6})$	Estimated Yield
$K^-\ \pi^+\ \pi^-$	$D\pi$ RS	55 ± 7 [14]	67.1±9.7
$K^+\ \pi^-\ \pi^-$	$D\pi$ WS	< 0.9 [16]	<1.1
$K^-\ \pi^+\ K^-$	DK RS	< 0.2 [16]	<0.2
$K^+\ \pi^-\ K^-$	DK WS	5.0 ± 0.7 [17]	6.0±0.8

IV. STUDY OF $B\overline{B}$ BACKGROUNDS

We study the $B\overline{B}$ background for each signal category ($D\pi$, $D^*\pi$ DK, D^*K) and charge combination (right-sign and wrong-sign) using a sample of $e^+e^- \to \Upsilon(4S) \to B\bar{B}$ MC events corresponding to about 3 times the data luminosity. In addition, dedicated Monte Carlo signal samples are used to estimate the background from $B^- \to Dh^-$ events and the background from the charmless decay $B^- \to K^+\pi^-K^-$. We identify three main classes of background events which can peak in $m_{\rm ES}$ inside the signal region and mimic the $D^{(*)}\pi$ and $D^{(*)}K$ signal:

1. Charmless B decays $B^- \to h^+h^-h^-$ $(h = \pi, K)$: we list in Table II the 3-body charmless decays affecting our analysis, their branching fractions [14] and the numbers of reconstructed events expected in the affected modes after the selection. Due to the particle identification criteria used in the analysis only decays with the same final state particles as our signal modes contribute significantly to the background. These events are indistinguishable from the $Dh^{\pm}$ signal if the $K^-\pi^+$ invariant mass is consistent with the D mass. The two decays affected by a significant charmless background are right-sign $B^- \to [K^-\pi^+]_D\pi^-$ and wrong-sign $B^- \to [K^+\pi^-]_DK^-$. Using $B^- \to K^-\pi^+\pi^-$ events selected in the $B\overline{B}$ Monte Carlo sample, we estimate the efficiency of $B^- \to K^-\pi^+\pi^-$ events to be reconstructed as a $[K^-\pi^+]_D\pi^-$ candidate as $(0.26 \pm 0.02)\%$. The corresponding background is estimated to be 67.1±9.7 events, where the error is dominated by the statistical uncertainty on the $B^- \to K^-\pi^+\pi^-$ branching fraction. The efficiency of $B^- \to K^+\pi^-K^-$ events to be reconstructed as $[K^+\pi^-]_DK^-$ WS candidates is determined from a high statistics dedicated $B^- \to K^+\pi^-K^-$ signal Monte Carlo sample, and is found to be $(0.27 \pm 0.01)\%$. The corresponding peaking background from $B^- \to K^+\pi^-K^-$ events mimicking $B^- \to [K^+\pi-]_DK^-$ WS decays is estimated to be 6.0±0.8 events, where the error is dominated by the statistical uncertainty on the $B^- \to K^+\pi^-K^-$ branching fraction. From a fit to data selected in the D mass sidebands, we cross-check this prediction and find 6.5±4.0 peaking events, in good agreement with the MC prediction. We also check that, because of the tight Δm cut applied to the D^* decay products, the $B^- \to D^*h^-$ channels are not affected by charmless peaking backgrounds.

2. Events of the type $B^- \to Dh^-$: this background is estimated by running the analysis on a sample of $B^- \to Dh^-$ signal MC events properly renormalised to the data sample, and fitting the $m_{\rm ES}$ spectra of the selected events to the sum of a Gaussian signal and a combinatorial background. We find that a peaking background of 2.6 ± 0.4 events is predicted in the $B^- \to [K^+\pi-]_DK^-$ WS channel. This component is dominated (2 events out of 2.6) by decays $B^- \to [K^-K^+]_D\pi^-$ failing the D mass veto and by WS decays $B^- \to [K^+\pi^-]_D\pi^-$ where the π^- is misidentified as a K^-. For the D^*K channels, the $B^- \to [K^-K^+]_D\pi^-$ contribution is suppressed by the Δm cut on the D^*-D mass difference, and the WS $D^*\pi$ contribution is 0.5±0.1 events for $D^* \to D\pi^0$ and 0.6±0.2 events for $D^* \to D\gamma$. Another background of the same type occurs in the right-sign DK decays. It consists of events $B^- \to [K^-\pi^+]_{D^{(*)}}\pi^-$ where the bachelor π^- is misidentified as a K^-, which fake the RS signal $B^- \to [K^-\pi^+]_{D^{(*)}}K^-$. This contribution is predicted by the simulation and has been verified in the data by fitting the ΔE spectrum of $D^{(*)}K$ candidates in the $m_{\rm ES}$ signal region, which shows a second peak due to $D^{(*)}\pi$ candidates, shifted by 50 MeV with respect to the signal.

3. Other decays: this component is estimated by fitting the $m_{\rm ES}$ spectra of $B\overline{B}$ MC events, after removing the charmless and $B^- \to Dh^-$ components. For $B^- \to [K^+\pi^-]_DK^-$ WS decays, the peaking component is estimated to be 4 ± 3 events, where the uncertainty is dominated by the statistical error on the simulated data. The main sources of peaking background which could be identified are listed in Table III. They include $\overline{B}^0 \to D^{*+}h^-$ reconstructed as $B^- \to D^{*0}h^-$, semi-leptonic decays $B^0 \to D^{**-}e^+\overline{\nu}_e$ ($D^{**-} \to \bar{D}^{(*)0}\pi^-$, $\bar{D}^0 \to K^+\pi^-$) where the e^+ is missed, faking the WS signal $B^- \to [K^+\pi^-]_{D^{(*)}}\pi^-$, and decays $B^- \to D^{(*)}\rho^-$ faking the RS signal $B^- \to [K^-\pi^+]_{D^{(*)}}\pi^-$.

A summary of the $B\overline{B}$ background studies is given in Table III, for $B \to D^{(*)}\pi$ and $B \to D^{(*)}K$. For each channel, the $m_{\rm ES}$ spectra of events selected in the $B\overline{B}$ MC simulation (after removing the corresponding signal) were fitted by the sum of a combinatorial background component and a peaking component, using the same parametrization described in Sec. III C. The average number of $B\overline{B}$ combinatorial and peaking background events predicted by the simulation are given in Table III, together with the main sources of peaking events and the

TABLE III: Expected numbers of signal and $B\overline{B}$ background events, peaking background parametrization and dominant sources of peaking backgrounds for $B \to D^{(*)}\pi$ and $B \to D^{(*)}K$. $N^{(comb)}_{B\overline{B}}$ is the combinatorial part of the background, parametrized by an ARGUS function, and $N^{(peak)}_{B\overline{B}}$ is the component peaking in $m_{\rm ES}$, parametrized by either a Gaussian function or a bifurcated Gaussian function. The average event yield expected for the WS signal is computed assuming $r^{(*)}_B = 10\%$ and no interference term ($\cos\gamma \times \cos\delta = 0$).

Mode	Signal yield	$N^{(comb)}_{B\overline{B}}$	$N^{(peak)}_{B\overline{B}}$	Peaking bkgd. parametrization	Peaking bkgd. sources
$D\pi^-$ WS	86	93.7±6.0	10.6 ± 3.0	Gaussian	$D_0^{*-}e^+\nu_e$
$D^*_{D\pi^0}\pi^-$ WS	31	24.7±8.3	29.0 ± 8.7	Bifurcated Gaussian	$D_0^{*-}e^+\nu_e$, $D_1^{'-}e^+\nu_e$
$D^*_{D\gamma}\pi^-$ WS	25	111±9	47 ± 7	Bifurcated Gaussian	$D_0^{*-}e^+\nu_e$, $D_1^{'-}e^+\nu_e$, and $D^{(*)0}\rho^0$
$D\pi^-$ RS	24240	307.3±11.7	222.0±10.3	Gaussian	$K^-\pi^+\pi^-$, $(c\bar{c})K^-$
$D^*_{D\pi^0}\pi^-$ RS	8931	620.7±33.7	507.3 ± 33.3	Bifurcated Gaussian	$D^*\rho^-$, $D^{**}\pi^-$
$D^*_{D\gamma}\pi^-$ RS	7242	1225±64	2432 ± 67	Bifurcated Gaussian	$D^*\rho^-$, $D^{**}\pi^-$, and $D^*_{D\pi^0}\pi^-$
DK^- WS	26.3	107.0±6.3	12.6 ± 3.1	Gaussian	Dh^-, $K^-K^+\pi^-$
$D^*_{D\pi^0}K^-$ WS	8.5	17.3±2.7	2.7 ± 1.6	Gaussian	—
$D^*_{D\gamma}K^-$ WS	6.8	68.3±5.3	6.0 ± 2.4	Gaussian	—
DK^- RS	1944	50.7±5.3	299.3±10.7	Gaussian	$D\pi^-$
$D^*_{D\pi^0}K^-$ RS	618	56.0±6.7	127.0 ± 8.3	Gaussian	$D^*_{D\pi^0}\pi^-$
$D^*_{D\gamma}K^-$ RS	503	66.0±14.7	326.7 ± 17.3	Bifurcated Gaussian	$D^*_{D\gamma}\pi^-$, $D^*_{D\pi^0}K^-$

functional shapes chosen to describe the peaking background. The numbers of signal events expected are also given for comparison. For the $B \to D^*K$ WS channels, we could not identify a specific source of peaking background due to the lack of statistics in the simulation. For all channels, we use the values of the peaking components summarized in Table III in the maximum likelihood fit. Statistical uncertainties in the expected yields are incorporated in the corresponding systematic uncertainties.

V. RESULTS

A. Results for $B \to D^{(*)}\pi$

The results for $B \to D^{(*)}\pi$ are displayed in Fig. 3 (right-sign modes) and Fig. 4 (wrong-sign modes). They are summarized in Table IV. Clear signals are observed in the $B \to D\pi$ and in the $B \to D^*_{D\pi^0}\pi$ WS modes, with statistical significances of 7σ and 4.8σ, respectively. The significance is defined as $\sqrt{-2\ln(\mathcal{L}_0/\mathcal{L}_{\rm max})}$, where $\mathcal{L}_{\rm max}$ and $\mathcal{L}_0$ are the likelihood values with the nominal and with zero WS signal yield, respectively. For $B \to D^*_{D\gamma}\pi$ WS decays, the significance is only 2σ, due to the large peaking background. Below we discuss the sources of systematic uncertainties that contribute to our $\mathcal{R}^{(*)}_{D\pi}$ measurements:

1. Signal NN shape: in the nominal fit, we use the NN PDF from the B signal MC. To estimate the related systematics, we refit the data using a signal NN PDF extracted from the high purity and high statistics $B \to D\pi$ RS data, after subtracting the residual continuum background contamination predicted by the simulation. We set the systematic uncertainty to the difference with the nominal fit result.

2. B background NN shape: from a study of generic $B\overline{B}$ MC, it appears that the NN spectra of B background events in the $m_{\rm ES}$-ΔE signal box are similar to the signal (but suffer from very low statistics), while the NN spectra of background events in an enlarged $m_{\rm ES}$-ΔE region differ significantly from the signal and show less peaking close to 1. In the nominal fit we assumed that both the peaking and the non-peaking $B\overline{B}$ background components could be described by the $B \to D\pi$ signal NN PDF. To estimate the related systematic error, we used $B\overline{B}$ generic background events selected in a ΔE-$m_{\rm ES}$ enlarged window $|\Delta E| < 200\,{\rm MeV}$ and $m_{\rm ES} > 5.20\,{\rm GeV}/c^2$ to build the NN PDF of the non-peaking part of the $B\overline{B}$ background (keeping the signal NN PDF to describe the peaking part of this background) and repeated the fits, taking the difference of the results as the associated systematic uncertainty.

3. Continuum background NN shape: to account for possible differences between the simulation and the data, we used the NN spectrum from off-peak data instead of $q\bar{q}$ MC ($q = u, d, s, c$) to model this component. We set the associated systematic uncertainty to the difference of the two results, but the error is dominated by the large statistical uncertainty on the off-peak data sample.

4. The shape parameters $\zeta^{(WS)}_B$ and $\zeta^{(RS)}_B$ of the ARGUS functions describing the suppressed and favored $B\overline{B}$ combinatorial background: in the nominal fits, these parameters are fixed to their values as

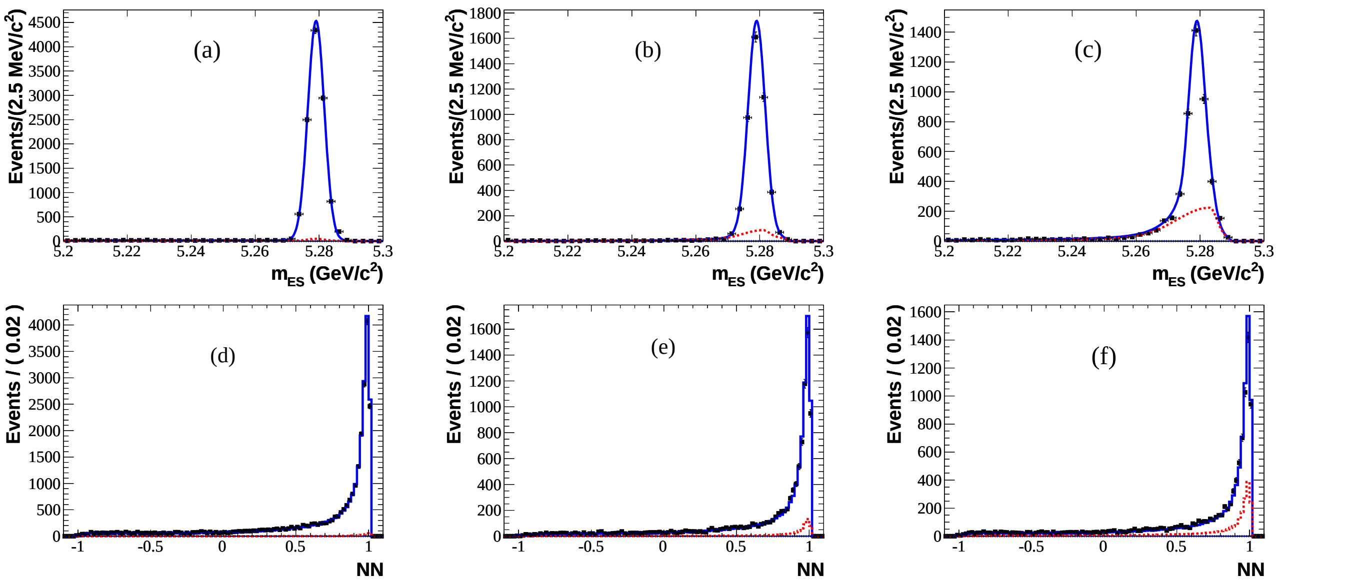

FIG. 3: (color online). Projections on m_{ES} (top) and NN (bottom) of the fit results for $D\pi$ (a,d), $D^{*}_{D\pi^0}\pi$ (b,e) and $D^{*}_{D\gamma}\pi$ (c,f) RS decays, for samples enriched in signal with the requirements $NN > 0.94$ (m_{ES} projections) or $5.2725 < m_{\mathrm{ES}} < 5.2875\ \mathrm{GeV}/c^2$ (NN projections). The points with error bars are data. The curves represent the fit projections for signal plus background (solid) and background (dashed).

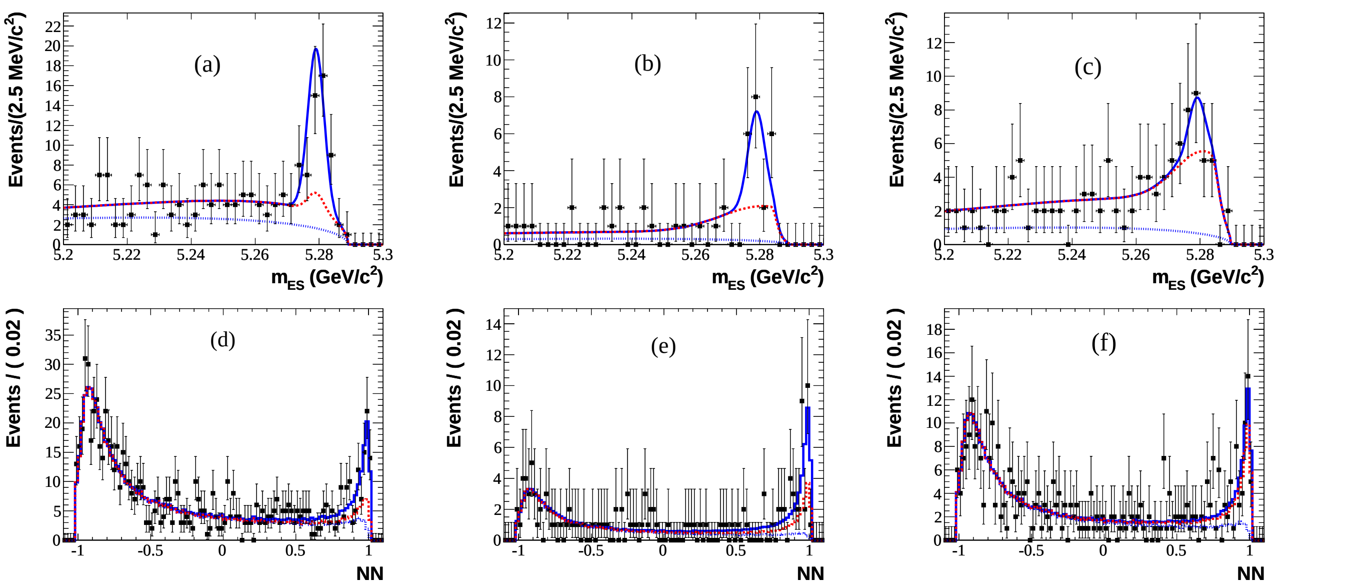

FIG. 4: (color online). Projections on m_{ES} (top) and NN (bottom) of the fit results for $D\pi$ (a,d), $D^{*}_{D\pi^0}\pi$ (b,e) and $D^{*}_{D\gamma}\pi$ (c,f) WS decays, for samples enriched in signal with the requirements $NN > 0.94$ (m_{ES} projections) or $5.2725 < m_{\mathrm{ES}} < 5.2875\ \mathrm{GeV}/c^2$ (NN projections). The curves represent the fit projections for signal plus background (solid), the sum of all background components(dashed), and $q\bar{q}$ background only (dotted).

determined from $B\overline{B}$ simulated events. To account for possible disagreement between data and simulation, we repeated the fits varying these parameters in a conservative range.

5. Peaking component in the B background: we varied the yield of the peaking component by $\pm 1\sigma$, where σ is either the statistical error from a fit to generic $B\overline{B}$ MC or the uncertainty on the branching fraction for known sources of peaking background.

TABLE IV: Summary of fit results for $D^{(*)}\pi$.

Mode	$D\pi$	$D^*_{D\pi^0}\pi$	$D^*_{D\gamma}\pi$
Ratio of rates, $\mathcal{R}^{(*)}_{D\pi}$ (10^{-3})	3.3 ± 0.6	3.2 ± 0.9	2.7 ± 1.4
Number of signal events N_{WS}	79.8 ± 13.8	28.3 ± 7.7	18.7 ± 9.7
Number of normalization events N_{RS}	24662 ± 160	9296 ± 102	7214 ± 105
B^+ ratio of rates, $\mathcal{R}^{(*)+}_{D\pi}$ (10^{-3})	3.2 ± 0.8	3.5 ± 1.2	4.6 ± 2.2
B^- ratio of rates, $\mathcal{R}^{(*)-}_{D\pi}$ (10^{-3})	3.4 ± 0.8	2.9 ± 1.2	1.0 ± 1.8
Asymmetry $\mathcal{A}^{(*)}_{D\pi}$	0.03 ± 0.17	-0.09 ± 0.27	-0.65 ± 0.55

6. Uncertainty on the number of $B\overline{B}$ combinatorial background events: in the $D^*\pi$ (and D^*K) fits where this component has been fixed, we vary it by $\pm 25\%$ (the level of agreement between data and simulation observed in the $D\pi$ and DK fits) and we take the difference with the nominal fit result as a systematic uncertainty.

The resulting systematic uncertainties are listed in Table V. We add them in quadrature and quote the results:

$$\begin{aligned}\mathcal{R}_{D\pi} &= (3.3 \pm 0.6 \pm 0.4) \times 10^{-3},\\ \mathcal{R}^*_{(D\pi^0)\pi} &= (3.2 \pm 0.9 \pm 0.8) \times 10^{-3},\\ \mathcal{R}^*_{(D\gamma)\pi} &= (2.7 \pm 1.4 \pm 2.2) \times 10^{-3},\end{aligned}$$

where the first uncertainty is statistical and the second is systematic. The values of $\mathcal{R}^{(*)}_{D\pi}$ are in good agreement with the world average $R_D = r_D^2 = \mathcal{B}(D^0 \to K^+\pi^-)/\mathcal{B}(D^0 \to K^-\pi^+)$, $R_D = (3.36 \pm 0.08) \times 10^{-3}$ [8].

A separate fit to B^+ and B^- candidates provides a measurement of the corresponding asymmetries. We obtain the following results:

$$\begin{aligned}\mathcal{A}_{D\pi} &= 0.03 \pm 0.17 \pm 0.04,\\ \mathcal{A}^*_{(D\pi^0)\pi} &= -0.09 \pm 0.27 \pm 0.05,\\ \mathcal{A}^*_{(D\gamma)\pi} &= -0.65 \pm 0.55 \pm 0.22,\end{aligned}$$

where the uncertainties are dominated by the statistical error. No significant asymmetry is observed for the $D^{(*)}\pi$ WS decays. The largest source of systematic uncertainty on the $D^{(*)}\pi$ asymmetries is from the uncertainty on the B background peaking component.

B. Results for $B \to D^{(*)}K$

The results for $B \to D^{(*)}K$ are displayed in Fig. 5 (RS modes) and Fig. 6 (WS modes). They are summarized in Table VI. Indications of signals are observed in the $B \to DK$ and in the $B \to D^*_{D\pi^0}K$ WS modes, with statistical significances of 2.2σ and 2.4σ, respectively (Fig. 7). Accounting for the systematic uncertainties, the significances become 2.1σ and 2.2σ, respectively. For $B \to D^*_{D\gamma}K$ WS, no significant signal is observed.

TABLE V: Summary of systematic uncertainties on $\mathcal{R}$ for $D^{(*)}\pi$, in units of 10^{-3}.

Source	$\Delta\mathcal{R}(10^{-3})$ $D\pi$	$\Delta\mathcal{R}(10^{-3})$ $D^*_{D\pi^0}\pi$	$\Delta\mathcal{R}(10^{-3})$ $D^*_{D\gamma}\pi$
Signal NN	± 0.1	± 0.1	± 0.1
$B\overline{B}$ background NN	± 0.1	± 0.1	± 0.9
$udsc$ background NN	± 0.1	± 0.1	± 0.3
$B\overline{B}$ comb. bkg shape (m_{ES})	± 0.2	± 0.1	± 0.2
Peaking background WS	± 0.2	± 0.8	± 2.0
Peaking background RS	± 0.0	± 0.1	± 0.1
$B\overline{B}$ comb. bkg	-	± 0.0	± 0.4
Combined	± 0.4	± 0.8	± 2.2

The systematic uncertainties have been estimated by testing different fit models and recomputing $\mathcal{R}^{(*)}_{DK}$, as explained in Section V A. A summary of the different systematic uncertainties is given in Table VII. The uncertainties on the NN describing the $B\bar{B}$ combinatorial background and the uncertainties on the $B\bar{B}$ peaking background are the two main contributions. For $B^\pm \to DK^\pm$, we find for the ratio of the WS to RS decay rates

$$\mathcal{R}_{DK} = (1.1 \pm 0.5 \pm 0.2) \times 10^{-2}.$$

Expressed in terms of event yields, the fit result is $19.4 \pm 9.6 \pm 3.5$ WS events. The results of fits to separate $B^+ \to DK^+$ and $B^- \to DK^-$ data samples are given in Table VI. Projections of the fits to B^+ and B^- data are shown in Figs. 8 and 9, respectively. We fit $\mathcal{R}^+_{DK} = (2.2 \pm 0.9 \pm 0.3) \times 10^{-2}$ for the B^+ sample, corresponding to $19.2 \pm 7.9 \pm 2.6$ events. On the contrary, no significant WS signal is observed for the B^- sample, and we fit $\mathcal{R}^-_{DK} = (0.2 \pm 0.6 \pm 0.2) \times 10^{-2}$. The statistical correlation between $\mathcal{R}^+_{DK}$ and $\mathcal{R}^-_{DK}$ (or $\mathcal{R}_{DK}$ and $\mathcal{A}_{DK}$) is insignificant.

The systematic errors on the asymmetries are estimated using the method discussed previously. The main systematic error on $\mathcal{A}_{DK}$ is from the uncertainty on the number of peaking B background events for the WS channel. This source contributes $^{+0.11}_{-0.14}$ to $\mathcal{A}_{DK}$, and $\pm 0.08 \times 10^{-2}$ to $\mathcal{R}_{DK}$, where the changes in the two

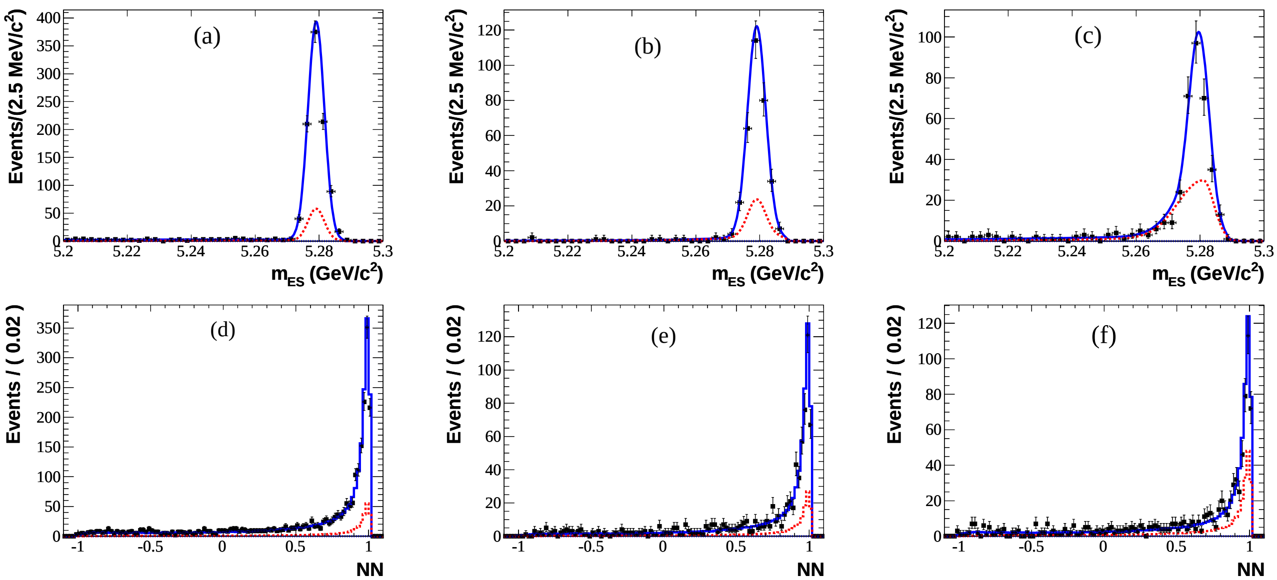

FIG. 5: (color online). Projections on $m_{\rm ES}$ (a, b, c) and NN (d, e, f) of the fit results for DK (a, d), $D^*_{D\pi^0}K$ (b, e) and $D^*_{D\gamma}K$ (c, f) RS decays, for samples enriched in signal with the requirements $NN > 0.94$ ($m_{\rm ES}$ projections) or $5.2725 < m_{\rm ES} < 5.2875\,{\rm GeV}/c^2$ (NN projections). The points with error bars are data. The curves represent the fit projections for signal plus background (solid) and background (dashed).

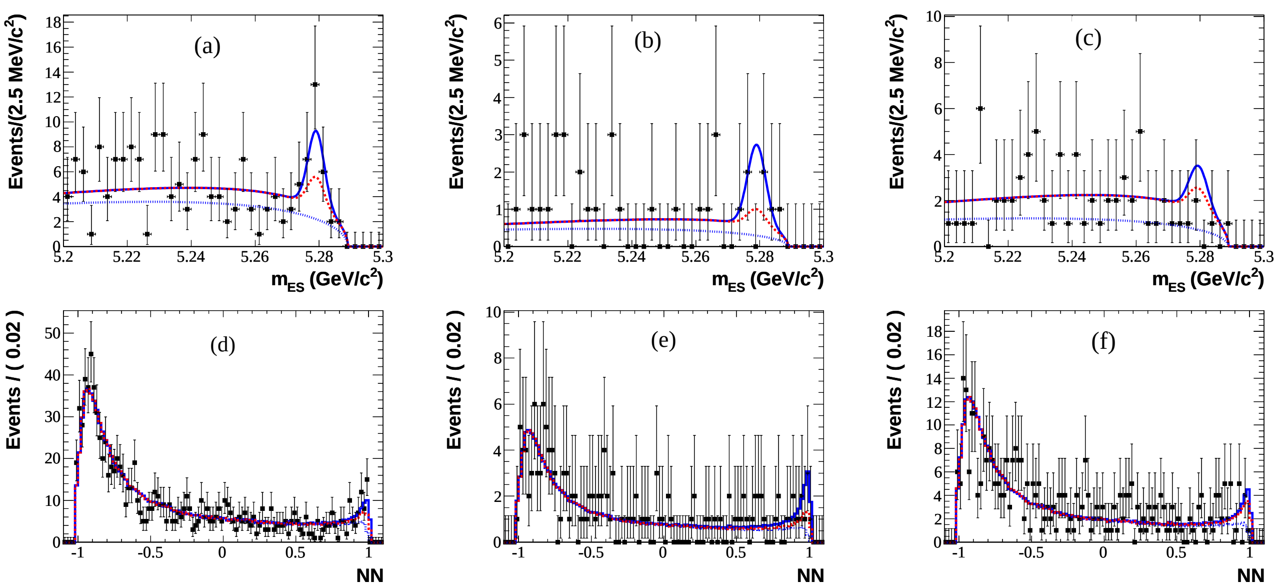

FIG. 6: (color online). Projections on $m_{\rm ES}$ (a, b, c) and NN (d, e, f) of the fit results for DK (a, d), $D^*_{D\pi^0}K$ (d, e) and $D^*_{D\gamma}K$ (c, f) WS decays, for samples enriched in signal with the requirements $NN > 0.94$ ($m_{\rm ES}$ projections) or $5.2725 < m_{\rm ES} < 5.2875\,{\rm GeV}/c^2$ (NN projections). The points with error bars are data. The curves represent the fit projections for signal plus background (solid), the sum of all background components (dashed), and $q\bar{q}$ background only (dotted).

quantities are 100% negatively correlated (increasing the peaking background increases $\mathcal{A}_{DK}$ but decreases $\mathcal{R}_{DK}$). The other sources of systematic uncertainty considered in Table VII are 100% correlated between $\mathcal{R}^+$ and $\mathcal{R}^-$, and mostly cancel in the asymmetry calculation. By comparing the number of B^+ and B^- events reconstructed in the $[K^\pm\pi^\mp]_D\pi^\pm$ analysis, where no significant asymmetry is expected, the uncertainty due to the detector charge asymmetry is estimated to be below the 1% level. Finally, we also account for a possible asymmetry of the

TABLE VI: Summary of fit results for $D^{(*)}K$.

Mode	DK	$D^*_{D\pi^0}K$	$D^*_{D\gamma}K$
Ratio of rates, $\mathcal{R}^{(*)}_{DK}$ (10^{-3})	11.1 ± 5.5	17.6 ± 9.3	13 ± 14
No. of signal events N_{WS}	19.4 ± 9.6	10.3 ± 5.5	5.9 ± 6.4
No. of normalization events N_{RS}	1755 ± 48	587 ± 28	455 ± 29
B^+ Ratio of rates, $\mathcal{R}^{(*)+}_{DK}$ (10^{-3})	21.9 ± 9.0	4.9 ± 7.9	9 ± 16
B^- Ratio of rates, $\mathcal{R}^{(*)-}_{DK}$ (10^{-3})	1.7 ± 5.9	37 ± 18	19 ± 23
Asymmetry $\mathcal{A}^{(*)}_{DK}$	-0.86 ± 0.47	0.77 ± 0.35	0.36 ± 0.94

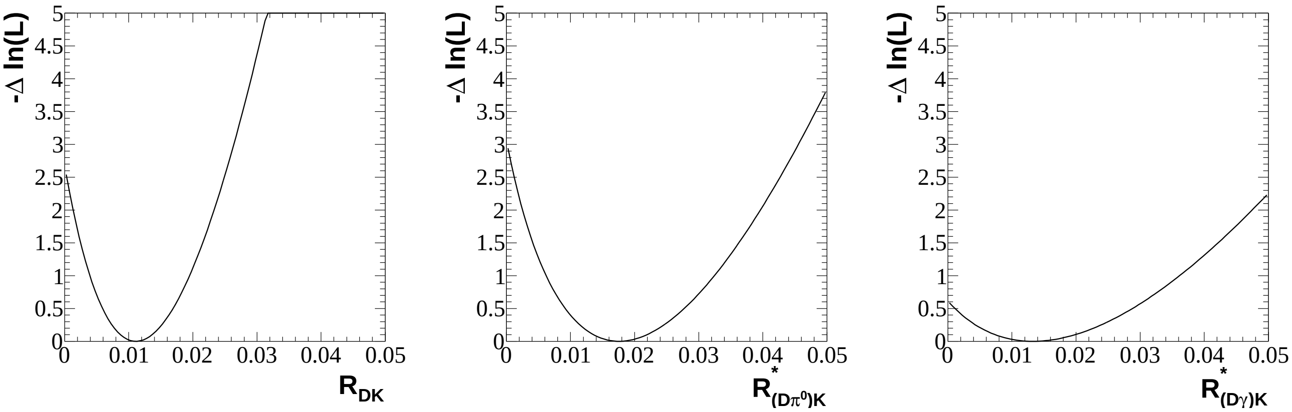

FIG. 7: Negative log-likelihood variation vs $\mathcal{R}^{(*)}_{DK}$ for $B^\pm \to DK^\pm$ (left), $B^\pm \to D^*_{D\pi^0}K^\pm$ (center) and $B^\pm \to D^*_{D\gamma}K^\pm$ (right). Systematic uncertainties are not included.

charmless $B^\pm \to K^\pm K^\mp \pi^\pm$ peaking background. The asymmetry of this background has been measured to be $0 \pm 10\%$ [17] and we estimate the corresponding systematic uncertainty by assuming a $\pm 10\%$ asymmetry of this background. The final result for the asymmetry is:

$$\mathcal{A}_{DK} = -0.86 \pm 0.47\ ^{+0.12}_{-0.16}\ .$$

TABLE VII: Summary of systematic uncertainties on $\mathcal{R}$ for $D^{(*)}K$, in units of 10^{-2}.

Error source	$\Delta\mathcal{R}(10^{-2})$	$\Delta\mathcal{R}(10^{-2})$	$\Delta\mathcal{R}(10^{-2})$
	DK	$D^*_{D\pi^0}K$	$D^*_{D\gamma}K$
Signal NN	± 0.1	± 0.1	± 0.3
$B\overline{B}$ background NN	± 0.1	± 0.3	± 0.4
$q\bar{q}$ background NN	± 0.1	± 0.1	± 0.1
$B\overline{B}$ comb. bkg shape ($m_{\rm ES}$)	± 0.1	± 0.1	± 0.1
Peaking background WS	± 0.2	± 0.3	± 0.6
Peaking background RS	± 0.0	± 0.1	± 0.1
Floating $B\overline{B}$ comb. bkg	-	± 0.1	± 0.2
Combined	± 0.2	± 0.4	± 0.8

For $B^\pm \to D^*_{D\pi^0}K^\pm$, we find for the ratio of the WS to RS decay rates

$$\mathcal{R}^*_{(D\pi^0)K} = (1.8 \pm 0.9 \pm 0.4) \times 10^{-2}.$$

Expressed in terms of event yields, the fit result is $10.3 \pm 5.5 \pm 2.4$ WS events. The results of fits to separate $B^+ \to D^*K^+$ and $B^- \to D^*K^-$ data samples are given in Table VI. Projections of the fits to B^+ and B^- data are shown in Figs. 8 and 9, respectively. We find $\mathcal{R}^{*-}_{(D\pi^0)K} = (3.7 \pm 1.8 \pm 0.9) \times 10^{-2}$ for the B^- sample, corresponding to $10.2 \pm 4.8 \pm 2.4$ events. On the contrary, no significant WS signal is observed for the B^+ sample, and we find $\mathcal{R}^{*+}_{(D\pi^0)K} = (0.5 \pm 0.8 \pm 0.3) \times 10^{-2}$. The systematic errors are estimated using the same method as for $B^\pm \to DK^\pm$, separately for B^+ and B^- events. The main systematic error on the asymmetry $\mathcal{A}^*_{(D\pi^0)K}$ is from the uncertainty on the number of peaking B background events for the WS channel. This source contributes ± 0.09 to $\mathcal{A}^*_{(D\pi^0)K}$, and $\mp 0.3 \times 10^{-2}$ to $\mathcal{R}^*_{(D\pi^0)K}$, where the two quantities are anti-correlated. The other sources of systematic uncertainties mostly cancel in the asymmetry calculation, because they induce relative changes on $\mathcal{R}^{*+}$ and $\mathcal{R}^{*-}$ which are 100% correlated. The final result for the asymmetry is:

$$\mathcal{A}^*_{(D\pi^0)K} = +0.77 \pm 0.35 \pm 0.12.$$

The asymmetry for $D^*_{D\pi^0}K$ has the opposite sign to the asymmetry for DK, in agreement with the shift of approximately 180° between δ_B and δ^*_B suggested by the measurements of Refs. [5, 7].

For $B \to D^*_{D\gamma}K$, we have no significant signal and fit

$$\mathcal{R}^*_{(D\gamma)K} = (1.3 \pm 1.4 \pm 0.8) \times 10^{-2}.$$

Expressed in terms of event yields, this result corresponds to $5.9 \pm 6.4 \pm 3.2$ events $D^*_{D\gamma}K$ WS. We fit 211 ± 19 RS B^- events and 244 ± 20 RS B^+ events, and find for the WS to RS ratios $\mathcal{R}^{*-}_{(D\gamma)K} = (1.9 \pm 2.3 \pm 1.2) \times 10^{-2}$ and $\mathcal{R}^{*+}_{(D\gamma)K} = (0.9 \pm 1.6 \pm 0.7) \times 10^{-2}$. The corresponding asymmetry is

$$\mathcal{A}^*_{(D\gamma)K} = +0.36 \pm 0.94^{+0.25}_{-0.41}.$$

VI. DISCUSSION

We use the $B^- \to D^{(*)}K^-$ analysis results and a frequentist statistical approach [18] to extract information on r_B and $r_B^{(*)}$. In this technique a χ^2 is calculated using the differences between the measured and theoretical values (including systematic errors) of the various ADS quantities from Eqs. (1), (4) and (5). We assume Gaussian measurement uncertainties. This assumption was checked to be valid and conservative at low r_B values with a full frequentist approach [5]. For $B^- \to DK^-$, we have for instance

$$\begin{aligned}\chi^2 &= (\mathcal{R}^+_{DK} - \mathcal{R}^{+(th)}_{DK}(r_B, \gamma, \delta_B, r_D, \delta_D))^2/\sigma^2_{\mathcal{R}^+} \\ &+ (\mathcal{R}^-_{DK} - \mathcal{R}^{-(th)}_{DK}(r_B, \gamma, \delta_B, r_D, \delta_D))^2/\sigma^2_{\mathcal{R}^-} \\ &+ (r_D^{(m)} - r_D)^2/\sigma^2_r \\ &+ (\delta_D^{(m)} - \delta_D)^2/\sigma^2_\delta, \end{aligned} \tag{9}$$

where $\mathcal{R}^{\pm(th)}_{DK}(r_B, \gamma, \delta_B, r_D, \delta_D)$ is given by Eq. (1), and where the two last terms constrain r_D and δ_D to the values $r_D^{(m)}$ and $\delta_D^{(m)}$ of Ref. [8] within their errors σ_r and σ_δ. The choice of ($\mathcal{R}^+_{DK}$, $\mathcal{R}^-_{DK}$) rather than ($\mathcal{R}_{DK}$, $\mathcal{A}_{DK}$) is motivated by the fact that the set of variables ($\mathcal{R}_{DK}$, $\mathcal{A}_{DK}$) is not well-behaved (the uncertainty on $\mathcal{A}_{DK}$ depends on the central value of $\mathcal{R}_{DK}$), while ($\mathcal{R}^+_{DK}$, $\mathcal{R}^-_{DK}$) are two statistically independent observables. In the same way, the two pairs of ADS observables ($\mathcal{R}^{*+}_{(D\pi^0)K}$, $\mathcal{R}^{*-}_{(D\pi^0)K}$) and ($\mathcal{R}^{*+}_{(D\gamma)K}$, $\mathcal{R}^{*-}_{(D\gamma)K}$) are used to extract r_B^*, while accounting for the relative phase difference in the two D^* decays [9]. We allow $0 \le r_B^{(*)} \le 1$, $-180° \le \gamma \le 180°$, and $-180° \le \delta_B^{(*)} \le 180°$. The minimum of the χ^2 for the $r_B^{(*)}$, γ, $\delta_B^{(*)}$, r_D, and δ_D parameter space is calculated first ($\chi^2_{\min}$). We then scan the range of $r_B^{(*)}$ minimizing the χ^2 (χ^2_{m}) by varying $\delta_B^{(*)}$, γ, r_D, and δ_D. A confidence level (C.L.) for r_B is calculated using $\Delta\chi^2 = \chi^2_{\mathrm{m}} - \chi^2_{\min}$ and one degree of freedom.

The results of this procedure are shown in Fig. 10 for the C.L. curve as a function of $r_B^{(*)}$. The results are summarized in Tab. VIII. For $B^- \to [K\pi]_D K^-$, we find the minimum χ^2 at $r_B = (9.5^{+5.1}_{-4.1})\%$. This leads to the upper limit: $r_B < 16.7\%$ at 90% C.L., to be compared to $r_B < 23\%$ at 90% C.L. for the previous ADS analysis as performed by BABAR [4] with 232×10^6 $B\overline{B}$ pairs, and to $r_B < 19\%$ at 90% C.L. for the corresponding ADS analysis as performed by Belle [6] with 657×10^6 $B\overline{B}$ pairs. We exclude $r_B = 0$ with a C.L. of 95.3%. Similarly, for $B^- \to [K\pi]_{D^*}K^-$ we find $r_B^* = (9.6^{+3.5}_{-5.1})\%$. This leads to the upper limit: $r_B^* < 15.0\%$ at 90% C.L., to be compared to $r_B^* < 16\%$ at 90% C.L. for the previous BABAR ADS analysis [4]. We exclude $r_B^* = 0$ with a C.L. of 83.9%.

TABLE VIII: Constraints on $r_B^{(*)}$ from the combined $B^- \to [K\pi]_{D^{(*)}}K^-$ ADS measurements.

Parameter	1 σ meas.	90% C.L. upper limit
r_B	$(9.5^{+5.1}_{-4.1})\%$	$< 16.7\%$
r_B^* from		
$D^{*0} \to D^0\pi^0$	$(13.1^{+4.2}_{-6.1})\%$	$< 19.5\%$
$D^{*0} \to D^0\gamma$	$(12.0^{+10.0}_{-12.0})\%$	$< 24.5\%$
all D^{*0} decays	$(9.6^{+3.5}_{-5.1})\%$	$< 15.0\%$

Using the above procedure we also determine the 2D confidence intervals for γ vs $\delta_B^{(*)}$ shown in Figs. 11 and 12. Choosing the solution with $0 < \gamma < 180°$ favors a positive sign for the strong phase δ_B ($\mathcal{A}_{DK} < 0$), and a negative sign for the strong phase δ_B^* ($\mathcal{A}^*_{(D\pi^0)K} > 0$). This result is in good agreement with the values of the strong phases determined in Refs. [5, 7]. Finally, Fig.13 shows the C.L. curve as a function of γ when combining the DK and D^*K results.

VII. SUMMARY

In summary, using a data sample of 467 million $B\overline{B}$ pairs, we present an updated search of the decays $B^- \to D^{(*)}K^-$ where the neutral D meson decays into the $K^+\pi^-$ final state (WS). The analysis method is first applied to $B^- \to D^{(*)}\pi^-$, where the D decays into the Cabibbo favored ($K^-\pi^+$) and doubly suppressed modes ($K^+\pi^-$). We measure $\mathcal{R}_{D\pi} = (3.3 \pm 0.6 \pm 0.4) \times 10^{-3}$, $\mathcal{R}^*_{(D\pi^0)\pi} = (3.2 \pm 0.9 \pm 0.8) \times 10^{-3}$ and $\mathcal{R}^*_{(D\gamma)\pi} = (2.7 \pm 1.4 \pm 2.2) \times 10^{-3}$, in good agreement with the ratio R_D of the suppressed to favored $D^0 \to K\pi$ decay rates, $R_D = (3.36 \pm 0.08) \times 10^{-3}$ [8]. Both the branching fraction ratios and the CP asymmetries measured for those modes, $\mathcal{A}_{D\pi} = (3 \pm 17 \pm 4) \times 10^{-2}$, $\mathcal{A}^*_{(D\pi^0)\pi} = (9 \pm 27 \pm 5) \times 10^{-2}$ and $\mathcal{A}^*_{(D\gamma)\pi} = (65 \pm 55\ ^{+20}_{-24}) \times 10^{-2}$, are consistent with the expectations discussed in Section I.

We see indications of signals for the $B \to DK$ and $B \to D^*_{D\pi^0}K$ wrong-sign modes, with significances of 2.1σ and 2.2σ, respectively. The ratios of the WS to RS

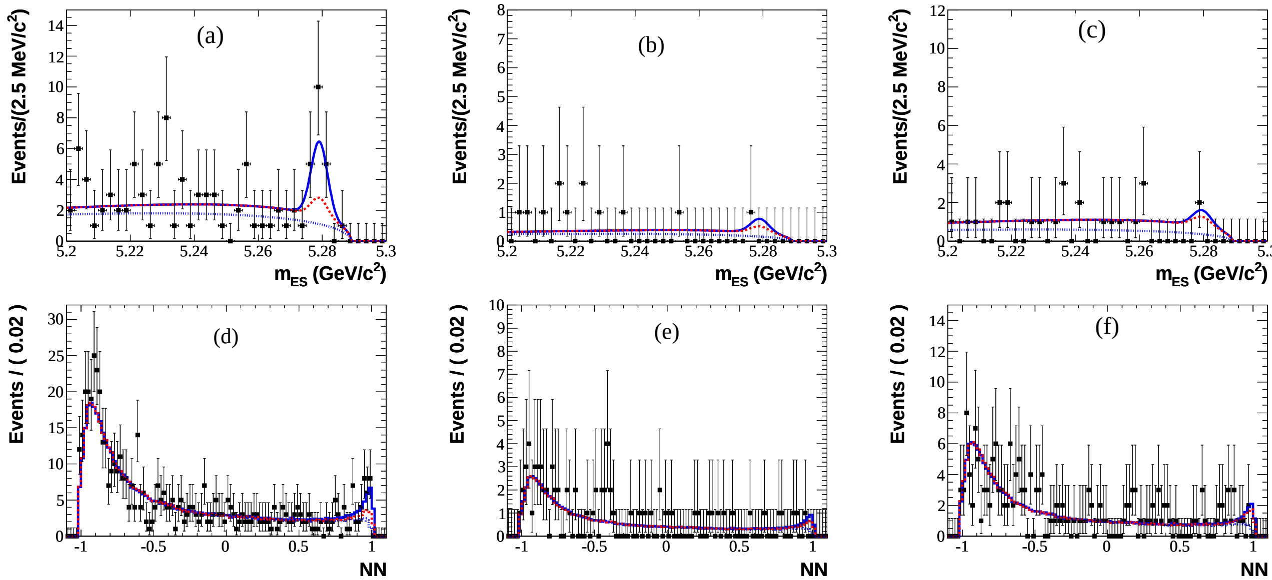

FIG. 8: (color online). Projections on m_{ES} (a, b, c) and NN (d, e, f) of the fit results for DK^+ (a, d), $D^*_{D\pi^0}K^+$ (b, e) and $D^*_{D\gamma}K^+$ (c, f) WS decays, for samples enriched in signal with the requirements $NN > 0.94$ (m_{ES} projections) or $5.2725 < m_{\mathrm{ES}} < 5.2875\,\mathrm{GeV}/c^2$ (NN projections). The points with error bars are data. The curves represent the fit projections for signal plus background (solid), the sum of all background components (dashed), and $q\bar{q}$ background only (dotted).

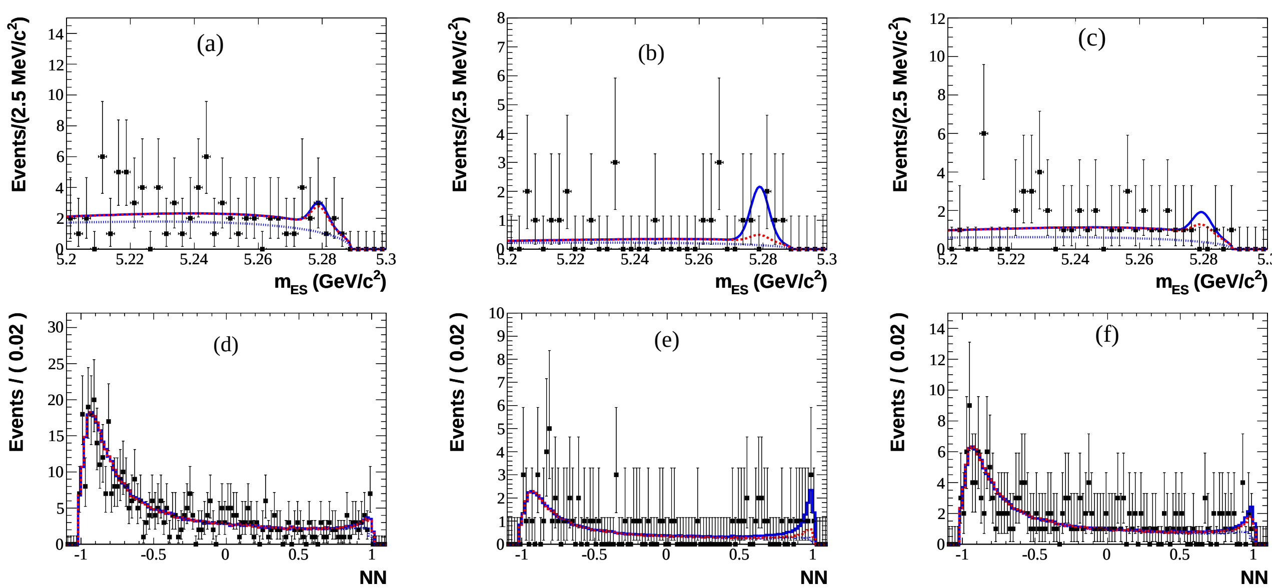

FIG. 9: (color online). Projections on m_{ES} (a, b, c) and NN (d, e, f) of the fit results for DK^- (a, d), $D^*_{D\pi^0}K^-$ (b, e) and $D^*_{D\gamma}K^-$ (c, f) WS decays, for samples enriched in signal with the requirements $NN > 0.94$ (m_{ES} projections) or $5.2725 < m_{\mathrm{ES}} < 5.2875\,\mathrm{GeV}/c^2$ (NN projections). The points with error bars are data. The curves represent the fit projections for signal plus background (solid), the sum of all background components (dashed), and $q\bar{q}$ background only (dotted).

branching fractions are measured to be $\mathcal{R}_{DK} = (1.1 \pm 0.5 \pm 0.2) \times 10^{-2}$ and $\mathcal{R}^*_{(D\pi^0)K} = (1.8 \pm 0.9 \pm 0.4) \times 10^{-2}$ for $B \to DK$ and $B \to D^*_{D\pi^0}K$, respectively. The separate measurements of $\mathcal{R}^{(*)\pm}_{DK}$ for B^+ and B^- events indicates large CP asymmetries, with $\mathcal{A}_{DK} = -0.86 \pm 0.47\ ^{+0,12}_{-0.16}$ for $B \to DK$ and $\mathcal{A}^*_{(D\pi^0)K} = +0.77 \pm 0.35 \pm 0.12$ for $B \to D^*K$, $D^* \to D\pi^0$. For the $B \to D^*_{D\gamma}K$ WS mode, we see no statistically significant evidence of a signal. We measure $\mathcal{R}^*_{(D\gamma)K} = (1.3 \pm 1.4 \pm 0.8) \times 10^{-2}$ and $\mathcal{A}^*_{(D\gamma)K} = +0.36 \pm 0.94\ ^{+0.25}_{-0.41}$. These results are used to extract the

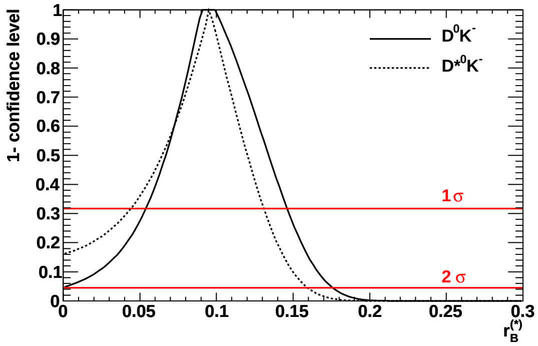

FIG. 10: (color online). Constraints on $r_B^{(*)}$ from the combined $B^- \to [K\pi]_{D^{(*)}}K^-$ ADS measurements. The solid (dotted) curve shows the 1 minus the confidence level to exclude the abscissa value as a function of $r_B^{(*)}$. The horizontal lines show the exclusion limits at the 1 and 2 standard deviation levels.

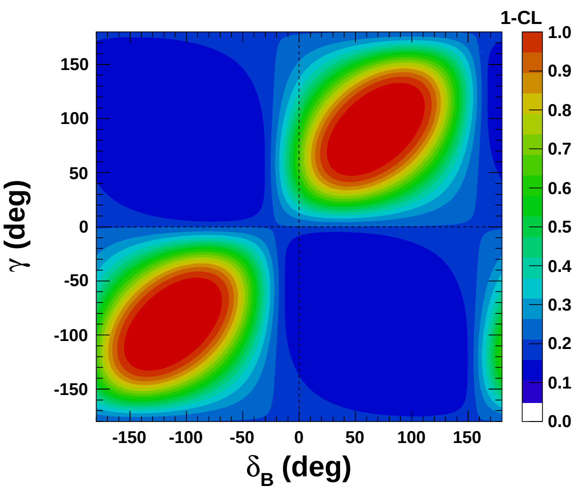

FIG. 11: (color online). One minus confidence level isocontours on γ vs δ_B from the $B^- \to [K\pi]_D K^-$ ADS measurement.

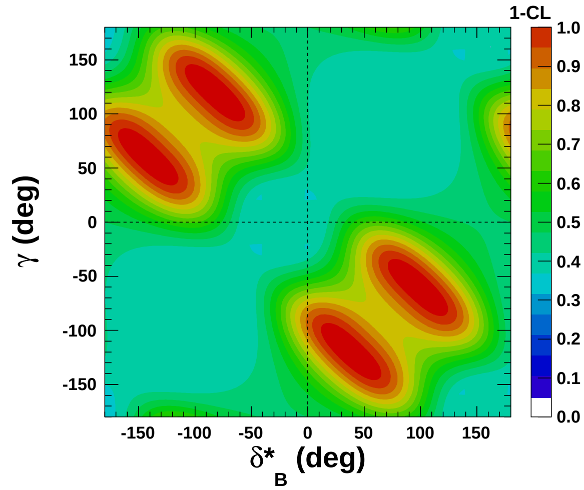

FIG. 12: (color online). One minus confidence level isocontours on γ vs δ^*_B from the combined $B^- \to [K\pi]_{D^*}K^-$ ADS measurements.

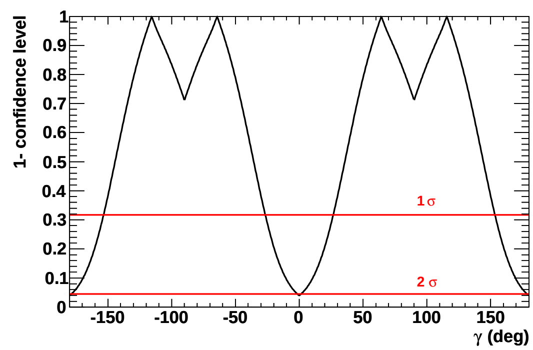

FIG. 13: (color online). Constraints on γ from the combined $B^- \to D^{(*)}[K^+\pi^-]K^-$ ADS measurements. The solid curve shows the (1-C.L.) to exclude the abscissa value. The horizontal lines show the exclusion limits at the 1 and 2 standard deviation levels.

following constraints on $r_B^{(*)}$:

$$\begin{aligned} r_B &= (9.5^{+5.1}_{-4.1})\%, \\ r^*_B &= (9.6^{+3.5}_{-5.1})\%. \end{aligned}$$

Assuming $0 < \gamma < 180°$, we also extract constraints on the strong phases $\delta_B^{(*)}$, in good agreement with other measurements Ref. [5, 7].

VIII. ACKNOWLEDGMENTS

We are grateful for the extraordinary contributions of our PEP-II colleagues in achieving the excellent luminosity and machine conditions that have made this work possible. The success of this project also relies critically on the expertise and dedication of the computing organizations that support BABAR. The collaborating institutions wish to thank SLAC for its support and the kind hospitality extended to them. This work is supported by the US Department of Energy and National Science Foundation, the Natural Sciences and Engineering Research Council (Canada), the Commissariat à l'Energie Atomique and Institut National de Physique Nucléaire et de Physique des Particules (France), the Bundesministerium für Bildung und Forschung and Deutsche Forschungsgemeinschaft (Germany), the Istituto Nazionale di Fisica Nucleare (Italy), the Foundation for Fundamental Research on Matter (The Netherlands), the Research Council of

Norway, the Ministry of Education and Science of the Russian Federation, Ministerio de Ciencia e Innovación (Spain), and the Science and Technology Facilities Council (United Kingdom). Individuals have received support from the Marie-Curie IEF program (European Union), the A. P. Sloan Foundation (USA) and the Binational Science Foundation (USA-Israel).

[1] N. Cabibbo, Phys. Rev. Lett. **10**, 531 (1963); M. Kobayashi and T. Maskawa, Prog. Theor. Phys. **49**, 652 (1973).
[2] L. Wolfenstein, Phys. Rev. Lett. **51**, 1945 (1983).
[3] D. Atwood, I. Dunietz, and A. Soni, Phys. Rev. Lett. **78**, 3257 (1997); Phys. Rev. D **63**, 036005 (2001).
[4] B. Aubert *et al.* (*BABAR* Collaboration), Phys. Rev. D **72**, 032004 (2005).
[5] P. del Amo Sanchez *et al.* (*BABAR* Collaboration), arXiv:1005.1096, submitted to Phys. Rev. Lett.
[6] Y. Horii *et al.* (Belle Collaboration), Phys. Rev. D **78**, 071901(R) (2008).
[7] A. Poluektov *et al.* (Belle Collaboration), arXiv:1003.3360, submitted to Phys. Rev. D.
[8] E. Barberio *et al.*, HFAG group, “Averages of b-hadron and c-hadron Properties at the end of 2007”, arXiv:0808.1297v3.
[9] A. Bondar and T. Gershon, Phys. Rev. D **70**, 091503(R) (2004).
[10] B. Aubert *et al.* (*BABAR* Collaboration), Nucl. Instrum. Methods Phys. Res., Sect. A**479**, 1 (2002).
[11] S. Agostinelli *et al.* (Geant4 Collaboration), Nucl. Instrum. Methods Phys. Res., Sect. A**506**, 250 (2003).
[12] D. Lange, Nucl. Instrum. Methods Phys. Res., Sect. A**462**, 152 (2001).
[13] T. Sjostrand, Comput. Phys. Commun. **82**, 74 (1994).
[14] C. Amsler *et al.* (Particle Data Group), Phys. Lett. B **667**, 1 (2008).
[15] The function is $\mathcal{A}(m_{ES}) \propto m_{ES}\sqrt{1-x^2}\exp[-\zeta(1-x^2)]$, where $x = 2m_{ES}/m_0$; H. Albrecht *et al.* (ARGUS Collaboration), Z. Phys. C **48**, 543 (1990).
[16] B. Aubert *et al.* (*BABAR* Collaboration), Phys. Rev. D **78**, 091102 (2008).
[17] B. Aubert *et al.* (*BABAR* Collaboration), Phys. Rev. Lett. **99**, 221801 (2007).
[18] J. Charles *et al.*, Eur. Phys. Jour. C **41**, 1 (2005) and updates at URL: http://www.slac.stanford.edu/xorg/ckmfitter